2010-08-09

Quantitative and Qualitative Results from Droplet Impingement Experiments on Superhydrophobic Surfaces with Micro-Ribs for Three Liquid Types

John T. Pearson
Brigham Young University - Provo

Quantitative and Qualitative Results from Droplet Impingement Experiments on Superhydrophobic Surfaces with Micro-ribs for Three Liquid Types

John T. Pearson

A thesis submitted to the faculty of
Brigham Young University
in partial fulfillment of the requirements for the degree of

Master of Science

Daniel Maynes, Chair
Brent W. Webb
Scott L. Thomson

Department of Mechanical Engineering

Brigham Young University

December 2010

ABSTRACT

Quantitative and Qualitative Results from Droplet Impingement

Experiments on Superhydrophobic Surfaces with

Micro-ribs for Three Liquid Types

John T. Pearson

Department of Mechanical Engineering

Master of Science

Experiments were performed in which liquid droplets were videographically recorded impacting horizontal superhydrophobic surfaces. The superhydrophobic surfaces were micropatterned with alternating ribs and cavities and coated with a hydrophobic coating. The following surface types were also tested for comparison: smooth uncoated, micropatterned uncoated, and smooth coated surfaces. Three liquid types were used: pure water, ethanol, and a 50/50 water/glycerine mixture. Acquired data demonstrated that the maximum droplet spread diameter exhibited a greater Weber number dependence than that previously reported in the literature. The time delays between impact and maximum spread and between impact and ejection of a vertical jet were characterized, and it was found that experiments with hydrophilic surface behavior follow somewhat different trends than those with hydrophobic behavior, and that there are modest differences between superhydrophobic and hydrophobic surfaces. When analyzing the velocity of the issuing vertical jet, a region of micro-jets was observed with velocities that, under certain conditions, can exceed 15 times the impact velocity. The experimental data acquired were also compared to two recent models from the literature and it was determined that the models do not adequately account for surface anisotropy or apparent slip at the solid-liquid interface. The experiments also showed that instabilities resulting in fingering are dependent upon surface and fluid type, but not contact angle. The onset of peripheral splashing was observed, in general, to occur at a lower Weber number as contact angle increased for the differing surfaces. For surfaces with rib and cavity features, the droplet spread and retraction were generally observed to be asymmetric with spread and retraction faster along the length of the ribs. The occurrence of two-pronged and oscillating jets for water/glycerine tests was also observed for all patterned surfaces. Lastly, an interesting spread pattern with four liquid droplets clustered at about 30° from the perpendicular direction was observed for all fluid types on patterned surfaces for high Weber numbers.

Keywords: John Pearson, superhydrophobic, droplet, impingement

ACKNOWLEDGMENTS

There are many people who have helped me in the process of writing this thesis. I am thankful for all the guidance and support I have received from Dr. Maynes and Dr. Webb, who helped me understand what it is to write a professional paper.

I am especially indebted to my wife, Kylee, for her love, patience, and support.

TABLE OF CONTENTS

LIST OF TABLES

LIST OF FIGURES

1 INTRODUCTION

1.1 Droplet Impingement on Superhydrophobic Surfaces

Superhydrophobic surfaces have been an object of much research interest of late due to their strong ability to repel water. A surface can be classified as superhydrophobic when a deposited droplet has a static contact angle of $\theta \geq 120^{\circ}$. This water repelling effect is created by generating a micro-roughness on a surface that is either natively hydrophobic or will then have a hydrophobic coating applied.

One experimental application where superhydrophobic surfaces are of interest is droplet impingement on horizontal, isothermal surfaces. There is a growing body of literature exploring the use of superhydrophobic surfaces in droplet impingement, including analytical and numerical work (for a full literature review, see sections 2.2 and 3.2). A close inspection of the literature reveals areas where a full understanding of the impingement process has not yet been obtained, and the purpose of the present research is to fill some of those gaps, especially regarding variable liquid properties and the use of hydrophobic surfaces that exhibit anisotropy.

1.2 Thesis Organization

The research will be presented as two stand-alone chapters that can be published independently in archival form. Since background, motivation, and review of previous work are included in these chapters, they are not repeated here. Most of the quantitative data obtained in

the experiments will be presented in Chapter 2. Data regarding maximum spread diameter, elapsed time between droplet impact and maximum spread and between impact and vertical jet ejection, and vertical jet velocity will be presented. Empirical and analytical models from the open literature will also be discussed and compared with the present data, with deficiencies in the models noted. Additional data, not presented in Chapter 2, is available in Appendix A.

Chapter 3 will focus on qualitative observations not captured by the data of Chapter 2. The effect of instabilities resulting in fingering and peripheral splash will be noted. Also, some interesting phenomena regarding asymmetric spreading and retraction will be made. Further quantitative observations regarding the vertical jet will also be noted. Finally, some interesting phenomena regarding satellite droplet formation will be discussed.

Finally, Chapter 4 will offer conclusions from this work and provide recommendations for future work.

2 INFLUENCE OF LIQUID TYPE ON DROPLET IMPACT ON SUPERHYDROPHOBIC SURFACES WITH MICRO-RIBS

2.1 Abstract

Droplet impingement experiments were performed on superhydrophobic surfaces micropatterned with alternating ribs and cavities and compared for the following surface types: smooth uncoated, micropatterned uncoated, and smooth coated surfaces. Experiments were performed using droplets of water, ethanol, and a 50/50 water/glycerine mixture. The maximum droplet spread diameter exhibited a greater Weber number dependence than that previously reported in the literature. The time delays between droplet impact and maximum spread and between impact and ejection of a vertical jet were characterized, and it was found that experiments with hydrophilic surface behavior follow somewhat different trends than those with hydrophobic behavior. Also, the time delay data showed modest differences between superhydrophobic and hydrophobic surfaces. When analyzing the issuing vertical jet velocity, a region of micro-jets was observed with velocities that, under certain conditions, exceed 15 times the impact velocity. This issuing jet was also observed to show strong dependence on the fluid type and the surface type. For fluids of greater viscosity the dynamics of the issuing jet were significantly affected by the surface isotropy of grooved superhydrophobic surfaces. The present data were also compared to two recent models from the literature and it was determined that the models do not adequately account for surface anisotropy or apparent slip at the solid-liquid interface.

2.2 Introduction

Superhydrophobic surfaces have been an object of much research interest of late due to their strong ability to repel water. A surface can be classified as superhydrophobic when a deposited droplet has a static contact angle of $\theta \geq 120^{o}$. This water repelling effect is created by generating a micro-roughness on a surface and then applying a hydrophobic coating. The micro-roughness on the surface can take the form of posts, carbon nanotube arrays, ribs, etc. (Rothstein, 2010).

Previous studies have shown that droplets moving across superhydrophobic surfaces experience much less frictional resistance for continued motion when compared to other surfaces (Yeomans and Kusumaatmaja, 2007). Further, both experimental and analytical work has shown that significant reduction in the drag may exist for continuous laminar flow through small channels with superhydrophobic walls (Lauga and Stone, 2003; Ou et al., 2004; Ou and Rothstein, 2005; Maynes et al., 2007; Davies et al., 2006; Lee et al., 2008; Byun et al., 2008; Woolford et al., 2009a). The topic of turbulent flows over superhydrophobic surfaces is also currently being investigated, with the results published to date showing varying degrees of drag reduction (Woolford, 2009b; Min and Kim, 2004; Fukagata and Kasagi, 2006; Martell et al., 2009; Jeffs et al., 2010).

Another area of current interest, and the focus of this paper, is the detailed, temporal dynamics of liquid droplets impinging on these surfaces. When a droplet impacts a superhydrophobic surface, it will spread radially in a thin sheet until the diameter reaches a maximum. Due to surface tension, the droplet will then collapse inwards on itself with a vertical jet issuing from the center. The droplet may completely detach from the surface and impact the surface again. There are many areas where this research is relevant. Liquid impingement

droplet impact has direct application in areas such as ink jet printing, spray cooling processes, spray coating, self-cleaning surfaces, and water-repellant applications (Yarin, 2006).

It has been shown previously that the elapsed time that a droplet is in contact with the surface, between impact and rebound, is not a function of impact velocity, but does vary with droplet diameter (Richard et al., 2002). Bouncing behavior has been related to spring behavior, and an analytical model based on this analogy has been made (Okumura et al., 2003). Other empirical and analytical models based on an energy balance approach have been made (Mao et al., 1997; Kim and Chun, 2001; Attane et al., 2007) and these will be discussed in greater detail later. A numerical study, using a front-tracking marker-chain method, has also been performed for droplets impacting superhydrophobic surfaces (Renardy et al., 2003). The numerical model demonstrated excellent agreement with experimental data.

Predicting the maximum droplet spread diameter has also been a topic of interest. The empirical and analytical models that have been presented predict this with varying degrees of accuracy (Attane et al., 2007). Using a numerical model to predict maximum spread diameter has been successful (Renardy et al., 2003), and it has been shown that the normalized maximum spread diameter for droplets impacting superhydrophobic surfaces scales as $We^{1/4}$ (Okumura et al., 2003; Clanet et al., 2004) where $We = \rho u_i^2 D_i/\sigma$ is the Weber number associated with the droplet impact, u_i is the droplet vertical velocity at impact, D_i is the droplet diameter at impact, ρ is the fluid density, and σ is the fluid surface tension. Also, it has been shown that depending on conditions, the impinging droplet might adhere to the surface, partially bounce, fully bounce, or splash peripherally; attempts have been made to predict the transition between these different impact regimes and identify the primary influencing factors (Bartolo et al., 2006; Reyssat et al., 2006; Wang et al., 2007; Jung and Bhushan, 2007; Rioboo et al., 2008; Jung and Bhushan, 2008;

Brunet et al., 2008). One study compared electrowetting to droplet impact tests and found a correlation in transition requirements for each type of experiment that is related to the micro-structuring (Brunet et al., 2008).

Most studies addressing droplet impact on superhydrophobic surfaces have been conducted with surfaces with either arrays of posts (Reyssat et al., 2006; Jung and Bhushan, 2007; Jung and Bhushan, 2008; Kannan and Sivakumar, 2008) or random surface roughness elements (Mao et al., 1997; Attane et al., 2007; Renardy et al., 2003; Clanet et al., 2004; Wang et al., 2007; Rioboo et al., 2008; Jung and Bhushan, 2008; Brunet et al., 2008; Lau et al., 2003). These methods of generating micro-roughness result in surfaces that are isotropic. One research group has shown that a surface with ribs and cavities responds differently to impacting droplets depending on whether the fluid is moving parallel to the ribs or transverse to the ribs (Kannan and Sivakumar, 2008a; Kannan and Sivakumar, 2008b). These studies, however, were performed on surfaces that either had a contact angle much less than the 120º required to be classified as superhydrophobic (Kannan and Sivakumar, 2008a), or had fairly moderate contact angles (up to 135º) (Kannan and Sivakumar, 2008b). Therefore, experimental results obtained using superhydrophobic surfaces comprised of ribs and cavities are of interest, especially at very high contact angles. Further, virtually all previous work on superhydrophobic surfaces used only water as the working fluid. Therefore, the influence of varying fluid properties has not fully been explored. The purposes of this paper are to explore the influence of fluid type, to explore the effect of anisotropic surfaces, and to compare data with existing models.

The scope of this paper is limited to isothermal droplet impact tests on superhydrophobic surfaces. The surfaces were structured with micro-ribs, and two different rib spacings were considered. The following surfaces were tested for comparison: surfaces with a hydrophobic

coating but no micro-roughness, microstructured surfaces with and without a hydrophobic coating, and surfaces with neither a coating nor micro-roughness. Three fluid types were considered: pure water, ethyl alcohol, and a mixture that is 50% glycerine and 50% water (based on mass). Following the description of the experimental methodology and the results obtained, a comparison between the results with relevant analytical models from literature will be presented. Some deficiencies in published models will be noted along with points of possible improvement.

2.3 Method

Experiments were performed exploring droplet impingement on flat, horizontal surfaces. The impingement event was imaged and recorded at a high frame rate and the images were analyzed to obtain surface position and velocity measurements. The experimental setup consisted of a hypodermic needle at an adjustable height that released a fluid droplet. Two sizes of needles were employed, resulting in two droplet sizes. The droplets were nominally 2.5 mm or 4 mm in diameter for pure water, 2 mm or 3 mm for alcohol, and 2.5 mm for the water/glycerine mixture. The droplet impinged on a horizontal test surface placed below the needle. The process was illuminated by LED lighting, and recorded with a high-speed camera. Since the impingement process is very rapid, it was imaged at a rate of 6000 frames/sec. Examples of images of water droplets impacting four surface types used in the present study are shown in Fig. 2-1. For the cases shown $We \approx 50$ and $Oh \approx 0.002$ (Oh defined below). The surfaces shown, from left to right, are: a smooth uncoated surface (hydrophilic), a smooth coated surface, a grooved uncoated surface, and a grooved coated (superhydrophobic) surface. The images display a pure water droplet a) upon impact (0 ms), b) as it spreads radially outward (1.3 ms), c) approximately when maximum spread diameter is reached (2.7 ms), d) as a vertical jet is

being ejected, except for the hydrophilic case (6.3 ms), and e-f) as any ejected jets continue to rise (8 ms and 15 ms). For the cases with a hydrophobic coating, the droplet has detached from the surface in frame f. The hydrophilic case is much different from the others since there is very little inward retraction and thus an extremely weak rebounding jet, if any. There are also small qualitative differences between the other three surface types. For the surfaces with no coating, the droplet adheres to the surface, even if there is a strong rebounding jet, as is the case with the grooved uncoated surface. All acquired images were analyzed using image analysis software developed for this purpose, and the following parameters were calculated: Weber number, $We = \rho u_i^2 D_i / \sigma$, Ohnesorge number, $Oh = \sqrt{We}/Re = \mu/\sqrt{\rho\sigma D_i}$ (where μ is the fluid viscosity and $Re = \rho u_i D_i / \mu$ is the impact Reynolds number), maximum droplet diameter, D_m, total time from droplet impact until the maximum diameter is reached, t_D, the time from droplet impact until the jet is issued, t_j, and the maximum velocity of the jet, u_j. The Ohnesorge number relates viscous forces to inertial and surface tension forces. Data acquired covered Weber numbers ranging from 1 to 500, and Ohnesorge numbers ranging from 0.002 to 0.015.

For each acquired image, the image analysis software determined the location of the left-most and right-most pixel occupied by the droplet. The difference of these values was used to determine the diameter of the droplet at any given stage of the impingement process. The pixel-physical conversion factor was determined by imaging a precision ruler, and values varied between 25 and 45 pixels/mm, depending on camera settings. The software also measured the top-most location of the droplet. Polynomials were fit to the position data as a function of time and these least-squares fits were differentiated to characterize the vertical velocity and the droplet spread velocity. The uncertainty associated with the measurements is described in Section 2.3.1.

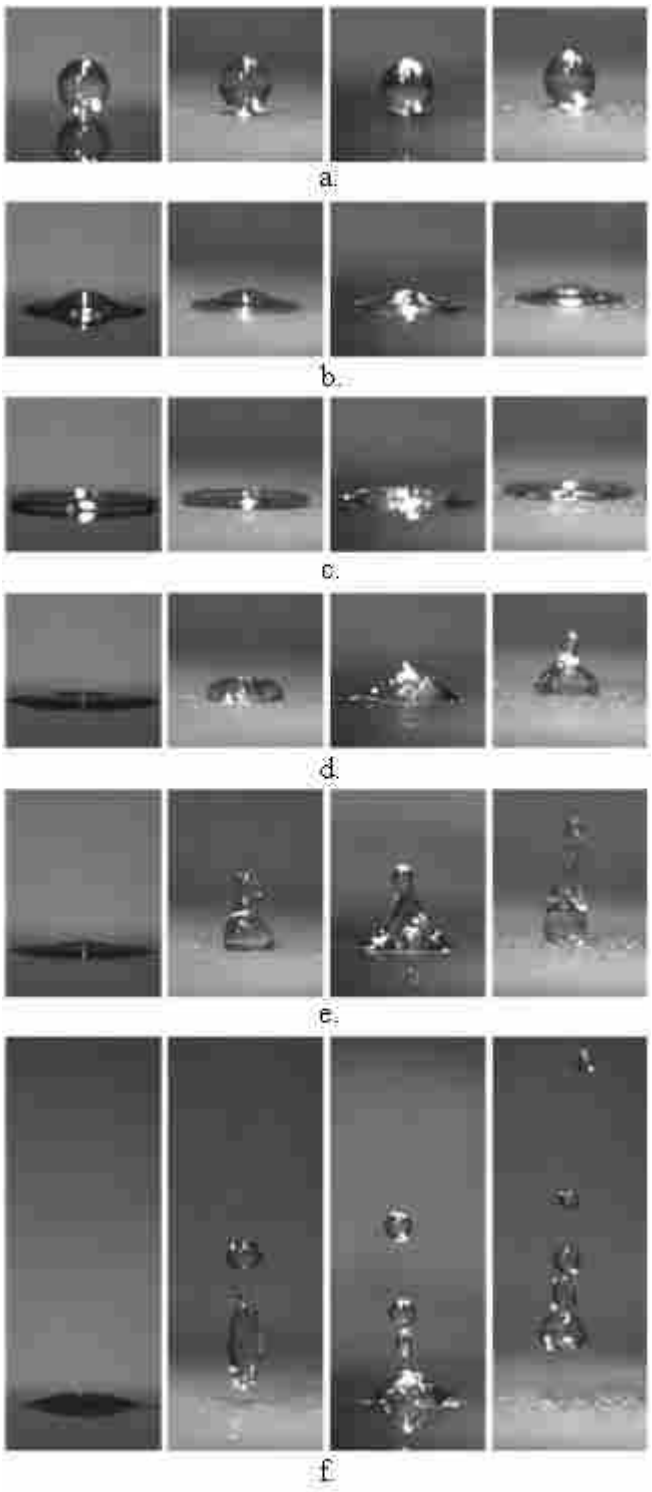

Figure 2-1: Images of water droplets impacting (from left to right) a smooth uncoated surface, a smooth coated surface, an uncoated microstructured surface, and a coated microstructured (superhydrophobic) surface. Images show the droplet at a) t = 0 ms, b) t = 1.3 ms, c) t = 2.6 ms, d) t = 6.3 ms, e) t = 8 ms, and f) t = 15 ms. For the cases shown $We \approx 50$.

In order to minimize experimental uncertainty, experiments were repeated two to six times and the results were averaged. The repeat experiments varied from each other by about 6% on average. Also, all dimensional data listed previously have been normalized using the impact velocity and diameter. Experiments were conducted with three different fluids: pure water (distilled), ethyl alcohol, and a 50/50 water/glycerine mixture. The fluid densities, viscosities, and surface tension values for the three different fluids are shown in Table 2-1. The ethyl alcohol has a much lower surface tension than water with a similar viscosity, while the water/glycerine mixture has a much higher viscosity than water with a similar surface tension.

Table 2-1: Density, viscosity, and surface tension for the three fluid types employed in the experiments.

Fluid Type	Density, ρ (kg/m^3)	Viscosity, μ (mPa·s)	Surface Tension, σ (mN/m)
Water (Incropera et al., 2006)	998	0.959	72.7
Ethyl Alcohol (Munson et al., 2006)	789	1.19	22.8
50% Glycerine 50% Water (Deng et al., 2007)	1126	5.9	69.2

As noted earlier, the structured surfaces had a micro-roughness in the form of alternating ribs and cavities. These were fabricated by standard photolithography and etching processes (Woolford et al., 2009b). The rib sidewalls are flat and are perpendicular to the bottom surface and the tops of the ribs are also flat and are parallel to the bottom surface. Two rib spacings were tested. The parameter that quantifies the spacing is the cavity fraction, F_c, defined as $F_c = w_c/w$, where w_c is the width of a cavity, and w is the combined rib and cavity width. The two cavity fractions tested in this work were 0.8 and 0.93. For the surface with $F_c = 0.8$ the ribs are 15 μm high and 8 μm wide. The ribs are separated by a cavity that is 32 μm wide. For the surface with $F_c = 0.93$ the ribs are 15 μm high and 2.75 μm wide. The ribs are separated by a

cavity that is 37.25 μm wide. For the purposes of the droplet impact experiments the ribs can be considered to be infinitely long, since the droplet never reaches the edge.

Because the rib and cavity features create frictional resistance and droplet contact angles that exhibit anisotropy, all droplet impingement tests were imaged from the two normal directions: as viewed when the fluid moves parallel to the ribs (the longitudinal direction), and perpendicular to the ribs (the transverse direction). For all surfaces and liquid types the liquid-solid contact angle was determined using a goniometer in both the longitudinal (L) and transverse (T) orientations. The contact angles, averaged over 10 measurements, for all surface types employed in the study are shown in Table 2-2.

Table 2-2: Contact angles in the longitudinal (L) and transverse (T) directions for all surfaces and fluids employed in the present study.

Case #	Coating	F_c	Droplet/Rib Orientation	Contact Angle, θ (º)		
				Water	Alcohol	Water-Glycerine Mixture
1	None	0	N/A	54.1	20	53.1
2	Fluoro	0	N/A	121.4	53.8	114.6
3	None	0.8	T	128.6	12.7	122
4	None	0.8	L	65	9	58.6
5	Fluoro	0.8	T	156.8	71	152.2
6	Fluoro	0.8	L	149.2	43.5	144.2
7	Teflon	0.93	T	161.9	74.8	156.6
8	Teflon	0.93	L	157.6	45	159.6

Two hydrophobic coatings were employed, Teflon and a fluoropolymer (a solution of Fluoropel M1604V and MQ000 (Woolford, 2009)) as indicated in the table. These coatings were applied by a spin-on process (Woolford et al., 2009b). Also, shown in the table is the

cavity fraction, F_c. As expected, the contact angle is greater when measured in the transverse direction (perpendicular to the ribs) than for the longitudinal direction. While this difference is not large when superhydrophobic behavior prevails (i.e., Cases 5-8 in Table 2-2 with water or water/glycerine mixture), the difference in θ in the two directions is significant for the uncoated structured scenarios (Cases 3-4) with either water or the water/glycerine mixture as the fluid type. Here θ is much greater when considering the transverse direction ($\theta > 120^o$) as compared to the longitudinal direction ($\theta < 70^o$). The alcohol exhibits wetting contact angles $\theta < 90^o$ for all surface types, but does exhibit significant variation between the two directions for the coated and structured surfaces (Cases 5-8).

2.3.1 Experimental Uncertainty

Uncertainty in the droplet Weber number arises from uncertainties in the measured impact velocity, u_i, the measured diameter at impact, D_i, and the uncertainty in fluid properties, ρ and σ. The impact velocity was characterized by least-squares fitting a second-order polynomial to the falling droplet position data as a function of time until impact occurs. The least-squares curve was then differentiated and evaluated at a time just prior to radial spreading of the droplet. Standard error analysis for least-squares regression fits (Weisberg, 2005) yields an error range from 0.1% to 1.5% in the impact velocity measurement. The diameter at impact was estimated by averaging the droplet side-to-side pixel difference for all frames prior to impact. The uncertainty associated with this measurement ranges from 0.3% to 1.5% with 95% confidence. Uncertainties in fluid properties are estimated to be ±0.2%. The overall uncertainty in each droplet Weber number measurement ranges from 1% to 3.2%.

Uncertainty in the normalized maximum spread diameter measurements arises from uncertainty in the measured maximum side-to-side displacements, D_m, and in the measurement

of diameter at impact, D_i. The uncertainties in the maximum displacements are estimated to be two pixels, and the overall uncertainty in the normalized maximum spread diameter data ranges from 3.3% to 7.7%.

The normalized time elapsed between impact and when the maximum droplet diameter is reached ($t_D u_i/D_i$), and the normalized elapsed time between droplet impact and when jet ejection occurs ($t_j u_i/D_i$) are influenced by the uncertainty in the measured impact velocity and diameter (u_i and D_i) and the uncertainty in the time measurements associated with each, t_D and t_j. The uncertainty in the time measurements is estimated to be one-half of the time delay between successive frames of data acquisition, and ranges from 2.1% to 3.8% for t_D and 1.1% to 1.6% for t_j. Overall uncertainties for the normalized elapsed time between droplet impact and maximum spread diameter range from 2.2% to 3.9% and for the normalized elapsed time between droplet impact and the jet ejection event range from 1.3% to 2.1%.

2.4 Results and Discussion

Case 1 in Table 2-2 represents the control case where a hydrophilic silicon surface without a hydrophobic coating or micro-structuring on the surface was employed. The dynamics in this case are those expected for a smooth hydrophilic surface (left set of images in Fig. 2-1). For this scenario, the droplet impacts, spreads radially, and adheres to the surface throughout the process. After spreading to a maximum diameter, surface tension pulls the droplet inwards until the droplet reaches an equilibrium state. When a hydrophobic coating is applied to the smooth surface (Case 2 and the second set of images from the left in Fig. 2-1) the droplet impacts, spreads radially and then collapses inwards due to surface tension pull, and a vertical jet forms. The droplet often separates into two volumes for this scenario with the larger volume of liquid

rebounding from the surface, while a smaller volume remains on the surface, although the entire droplet is observed to detach from the surface on occasion as seen in Fig. 2-1. When there is no coating applied, but micro-structuring has been added (Cases 3-4 and third set of images from the left in Fig. 2-1), the droplet spreads to a greater extent parallel to the ribs (longitudinal direction) than in the direction perpendicular to the ribs (transverse direction). Under this condition the ribs provide greater resistance to motion in the transverse direction and the surface tension pull is much greater in the longitudinal direction, concomitant with the difference in the contact angles for the two directions (see Table 2-2). As in Case 1, the liquid throughout the entire process adheres to the surface. For the surfaces exhibiting superhydrophobic behavior (Cases 5-8 and far right set of images in Fig. 2-1), the droplet spreads, collapses on itself, forms a vertical jet, and generally rebounds completely, leaving no fluid attached to the surface.

For all scenarios when water is the working fluid, other than the control case, as the maximum droplet spread diameter is reached much smaller scale satellite droplets may form that detach from the primary droplet volume. Shown in Fig. 2-2 is an illustration of this phenomenon for a water droplet impacting a superhydrophobic surface (Case 6). Images show the droplet a) at impact (rib orientation shown also), b) as it spreads and begins releasing satellite droplets (indicated), c) as it reaches a maximum spread, d) as a jet begins to form, e-f) as the jet continues upward. In images d-f some of the satellite droplets that have detached from the main mass can be seen. When comparing Figs. 2-1 and 2-2, it can be seen that the rebound of the droplet is much weaker in the case when peripheral splashing occurs. This has been observed in this study to occur for $We > 200$. The value of *We* where this behavior prevails varies slightly for the different surface types; the determination of the transition *We* has been the object of much study (Bartolo et al., 2006; Reyssat et al., 2006; Wang et al., 2007; Jung and Bhushan, 2007; Rioboo et

al., 2008; Jung and Bhushan, 2008; Brunet et al., 2008). No satellite droplet formation was observed for the water tests on the uncoated smooth surface (Case 1). When alcohol was used as the droplet liquid, satellite droplets formed at nominally the same *We*, although for the alcohol tests satellite droplet formation was also observed with the uncoated smooth surface (Case 1). When the water/glycerine mixture was utilized, satellite droplet formation was observed at higher *We* than for the other fluid types explored ($We > 250$), and was observed on all surface types. This delay can be attributed to the significantly higher viscosity of the water/glycerine mixture. When satellite droplet formation occurs the dynamics of the spreading and collapse are significantly impacted. Consequently, data from experiments where this phenomenon occurs are omitted from the subsequent results, except for the jet ejection data (Fig. 2-7 to Fig. 2-10).

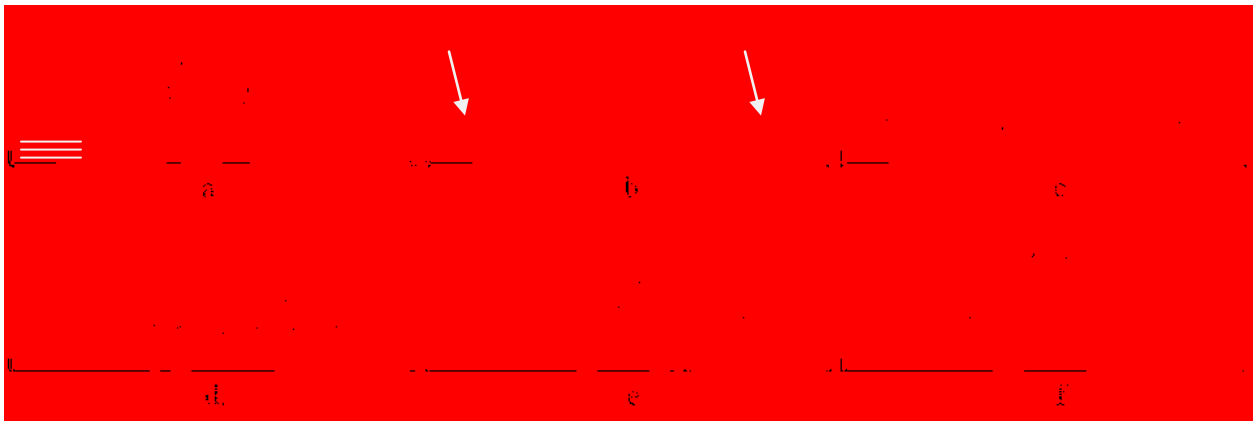

Figure 2-2: Images depicting a droplet that splashes peripherally. Frames show a water droplet a) at impact on a superhydrophobic surface (0 ms), b) as it is spreading radially and releasing satellite droplets (1.3 ms), c) as the droplet reaches maximum spread and begins collapsing (5.5 ms), d) after the droplet has collapsed and is forming a jet (13.8 ms), and e-f) as the droplet further rebounds from the surface (16 ms and 18.5 ms). Images were taken on a superhydrophobic surface with F_c = 0.8 (Case 6). Rib orientation is indicated in frame a.

2.4.1 Maximum Spread Diameter

Shown in Fig. 2-3 is the normalized maximum spread diameter, D_m/D_i, as a function of *We* for all three fluid types. These data correspond to a surface with F_c = 0.93 and a Teflon coating (Cases 7-8). Results for droplet spread in both the transverse (T) and longitudinal (L) directions are shown. For all fluid types and droplet sizes the D_m/D_i ratios follow a similar curve, with the exception of the data for alcohol spreading in the longitudinal direction. When spreading in the longitudinal direction (parallel to the ribs, Case 8), the alcohol spreads to a much greater extent at low Weber numbers than the other fluid types, or for alcohol spreading in the transverse direction. Recall from Table 2-2 that the alcohol-surface contact angle in this case is θ = 45°. Here, the alcohol is drawn down the ribs by surface tension. Conversely, in the transverse direction where the alcohol-surface contact angle is θ = 74.8°, the D_m/D_i ratio for the alcohol is nominally the same as for both water and the water/glycerine fluids, which exhibit much larger contact angles. At *We* > 100, the curves for the different fluid types and spread directions separate to a greater extent than at lower *We*, where they are all essentially the same (with the exception of the alcohol data in the longitudinal direction).

For the case of pure water the D_m/D_i ratio data for the two spread directions begin to diverge after *We* ≈ 100, where it can be seen that the droplet spread is greater in the longitudinal direction. One implication of this is that at higher *We* the droplet spreads in an elliptical manner, rather than circular. There is also modest elliptical spreading in the water/glycerine data at *We* > 100, where the D_m/D_i ratios are larger in the longitudinal direction than in the transverse direction.

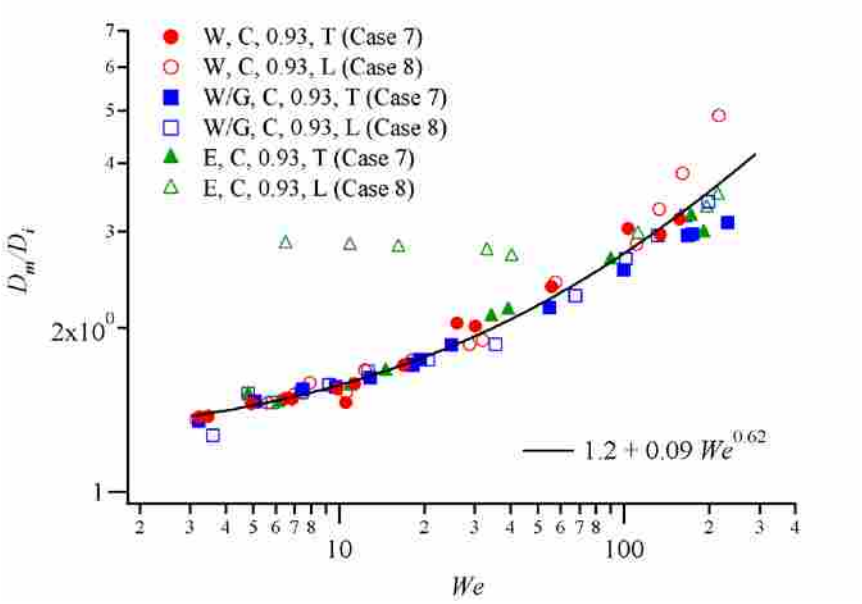

Figure 2-3: Normalized maximum spread diameter, D_m/D_i, as a function of *We* for all three fluid types on a superhydrophobic surface with F_c = 0.93 (Cases 7-8). Legend code is fluid type (W – water, W/G – water/glycerine mixture, E – ethanol), coated or uncoated (C – coated, U – uncoated), cavity fraction (0 – no grooves, F_c = 0.8 or 0.93), and spread direction (L – longitudinal, T – transverse).

Figure 2-4 shows a comparison of the normalized maximum spread diameter, D_m/D_i, as a function of *We* for water droplets impinging on the following surface types: uncoated smooth, coated smooth, and superhydrophobic (Cases 1, 2 and 5-8). Again, results are shown for spread in both the longitudinal and transverse directions. For all surface types the D_m/D_i ratio follows a similar curve, with the exception of the smooth uncoated surface (Case 1). For this case, the water-surface contact angle is θ = 54.1° which is significantly lower than for the other surfaces and typifies hydrophilic behavior. Again, at high *We* the droplets appear to spread somewhat further in the longitudinal direction than in the transverse direction. When examining the trends for D_m/D_i, a least-squares power-law fit to the data sets (shown on Figs. 2-3 and 2-4) reveals that for the uncoated smooth case, the D_m/D_i ratio scales as $We^{0.3}$. For the hydrophobic surfaces (θ > 90°) the D_m/D_i ratio scales as $We^{0.62}$ for both spread directions. The power-law exponent here is significantly larger than that reported by Okumura et al. (2003) and Clanet et al. (2004) who

observed $D_m/D_i \sim We^{1/4}$ for isotropic superhydrophobic surfaces. The $We^{1/4}$ relationship was assumed to hold for low viscosity fluids when $We > 1$, and assumed the form $D_m/D_i = AWe^B$. A least-squares fit to the present data for this form ($D_m/D_i = AWe^B$) is shown on Fig. 2-4, and features the same exponent as reported by Okumura et al. (2003) and Clanet et al. (2004). When an offset is allowed in fitting a power-law curve to the data ($D_m/D_i = AWe^B + C$), the data are better correlated, with the average error in the curve fit markedly reduced. The superhydrophobic surfaces in this study were anisotropic due to the grooves. However, the smooth coated case (Case 2) is isotropic, although not superhydrophobic, and the data follows the same trends as the data for the superhydrophobic cases (Cases 5-8).

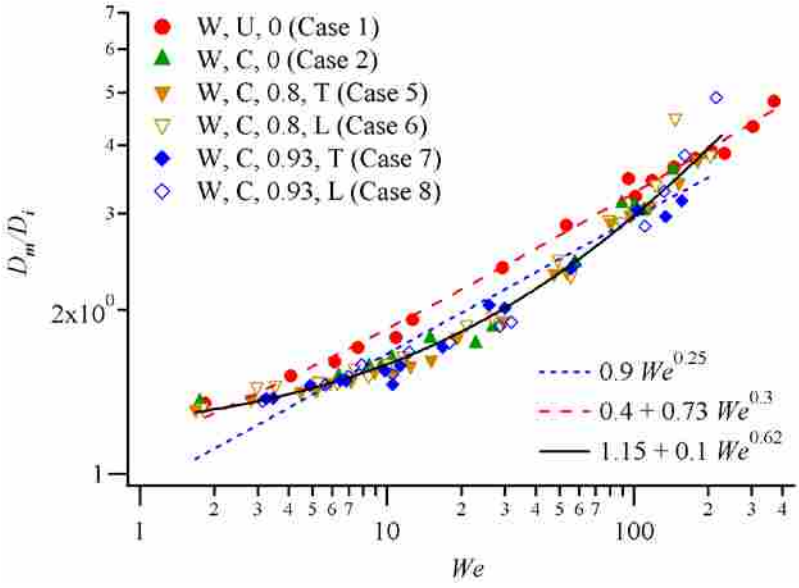

Figure 2-4: Normalized maximum spread diameter, D_m/D_i, as a function of *We* for water droplets impinging on four surfaces tested (Cases 1, 2, 5-8). See Fig. 2-3 caption for legend key.

2.4.2 Time to Maximum Spread

Shown in Fig. 2-5 is the time delay between the droplet impact and the point where the maximum spread diameter is attained, $t_D u_i/D_i$, as a function of *We* for all three fluid types. These

data correspond to a surface with F_c = 0.93 and a Teflon coating (Cases 7-8). Similar to the D_m/D_i data shown in Fig. 2-2, the $t_D u_i/D_i$ ratios follow a similar trend for both pure water and the water/glycerine mixture. Again, no dependence on droplet size is observed. The ethanol data corresponding to the longitudinal view again shows significant deviation from the other scenarios. For this configuration where $\theta < 90°$ the time from impact until the droplet reaches its maximum spread is greater than for all other scenarios. The difference is more pronounced at lower *We*. For all other scenarios the data follow a similar curve with no evidence of systematic deviation based on fluid type. One implication of the results for the alcohol data is that the droplet has reached its maximum diameter in the transverse direction while continuing to spread in the longitudinal direction. A least-squares curve fit to the data (excluding the alcohol in the longitudinal direction case) reveals that $t_D u_i/D_i \sim We^{0.39}$.

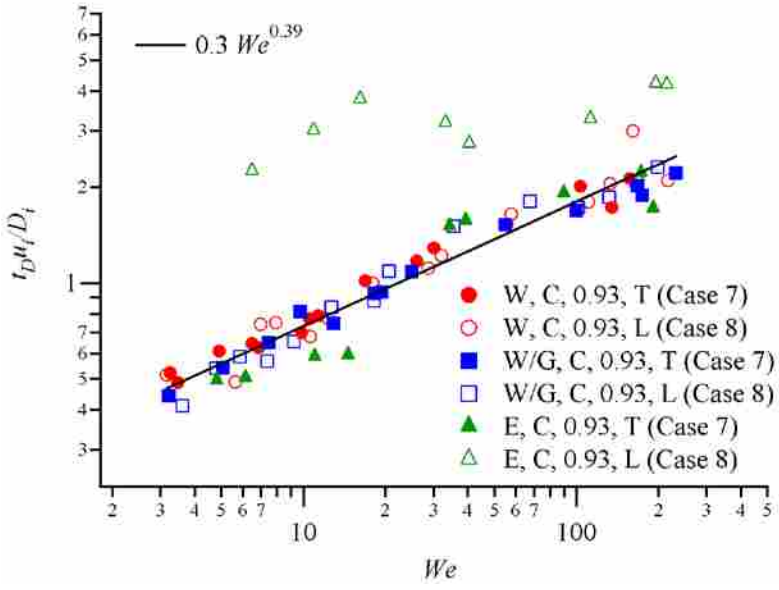

Figure 2-5: Normalized time delay between droplet impact and the point when the maximum spread diameter is attained, $t_D u_i/D_i$, as a function of *We* for all three fluid droplet types on a superhydrophobic surface with F_c = 0.93 (Cases 7-8). See Fig. 2-3 caption for legend key.

Figure 2-6 provides a comparison of the normalized time from droplet impact until the maximum spread diameter is attained, $t_D u_i/D_i$, as a function of *We* with water employed for Cases 1, 2, 4, 6, and 8. The data reveal that the general behavior for $t_D u_i/D_i$ is similar for the cases in the hydrophobic regime (Cases 2, 6, and 8) as well as for Case 4, which has θ = 65°. This is perhaps due to the influence of the hydrophobic contact angle in the transverse direction on this surface. A least-squares curve fit through the data for these surface types suggests that $t_D u_i/D_i \sim We^{0.4}$. Similar to the D_m/D_i data of Fig. 2-4, $t_D u_i/D_i$ is significantly larger for the uncoated smooth case (Case 1) than for the other scenarios shown. It can also be seen that at higher *We*, the superhydrophobic surfaces (Cases 6 and 8) have a moderately shorter time between impact and maximum spread diameter than the other cases.

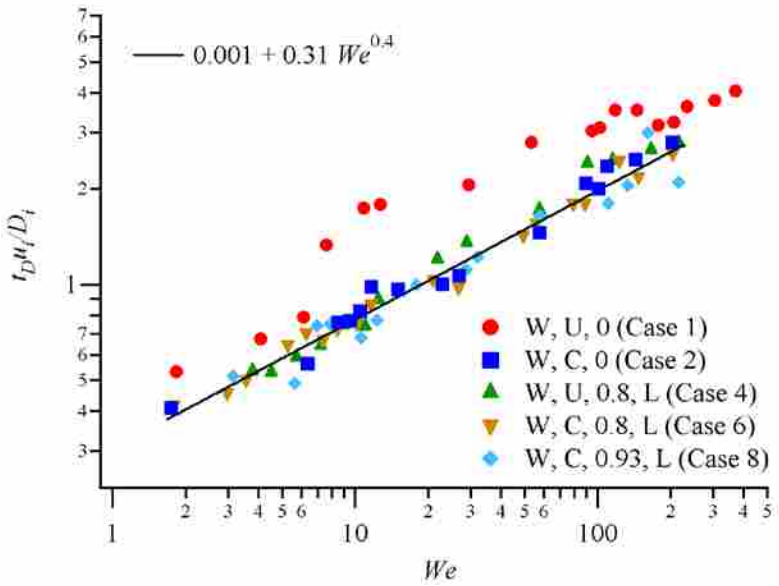

Figure 2-6: Normalized time delay between droplet impact and the point when the maximum spread diameter is attained, $t_D u_i/D_i$, as a function of *We* for water droplets impinging on each of the surfaces tested and in the longitudinal direction where applicable (Cases 1, 2, 4, 6, and 8). See Fig. 2-3 caption for legend key.

2.4.3 Time to Jet Ejection

The time difference between droplet impact and the time when the vertical liquid jet forms, $t_j u_i/D_i$, is the same when observed in the longitudinal and transverse spread directions for any given experiment. Thus, for all scenarios the results obtained from corresponding experiments in the two spread directions are averaged to decrease the overall uncertainty in determining this parameter. The ejecting jet has a maximum velocity immediately upon forming, and the time the jet was issued was determined by finding the time the maximum vertical velocity was reached. Shown in Fig. 2-7 is the normalized jet ejection time, $t_j u_i/D_i$, as a function of *We* for all three liquid types. These data were taken on a superhydrophobic surface, with F_c = 0.8. As illustrated by the data of Fig. 2-7, the results for the water and the water/glycerine mixture droplets coincide. This coincidental behavior was observed for all surface types explored. A least-squares power-law fit through the data reveal that $t_j u_i/D_i \sim We^{0.56}$ for water and water/glycerine droplets on this surface. The data derived from the alcohol droplet tests also exhibit a power-law dependence, with $t_j u_i/D_i \sim We^{0.71}$. It should be noted that the "jet" that is issued for the alcohol droplets is not really so much a jet as it is a mild upward movement of fluid at the center of the droplet. This movement typically represents a very small magnitude in vertical velocity. For ethanol droplets, wetting behavior prevails and a radial collapse due to surface tension pull is not a dominant mechanism. Also, the data do not reveal any dependence on droplet size.

Figure 2-8 illustrates how $t_j u_i/D_i$ is affected by surface type. Data for tests using pure water on each of the surfaces are shown. For $We < 20$, there is no significant difference between the trends for the different surfaces, other than for Case 1, the smooth uncoated surface. However, as *We* continues to increase, greater spread in the data prevails. At high *We* the data

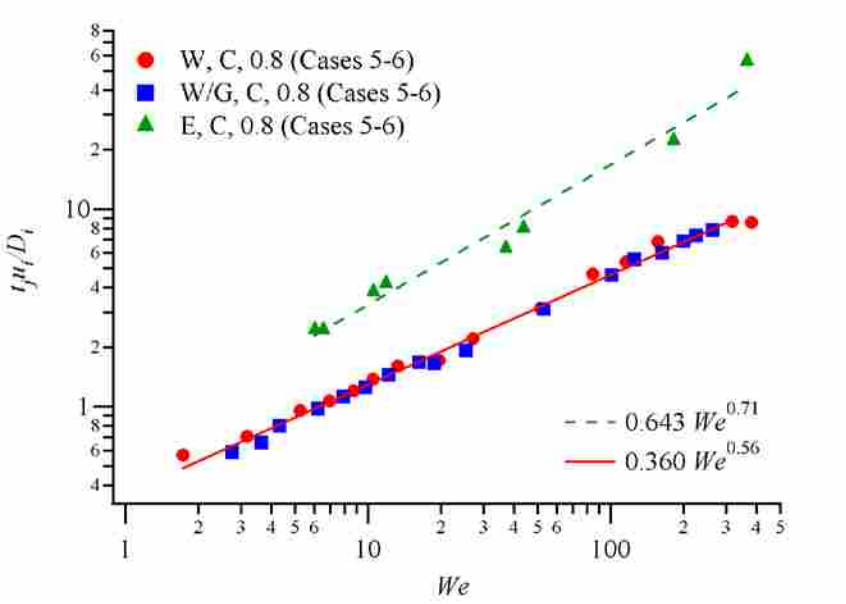

Figure 2-7: Normalized time difference between droplet impact and the point when the liquid jet forms, $t_j u_f / D_i$, as a function of *We* for all three liquid droplet types impinging on a superhydrophobic surface with F_c = 0.8 (Cases 5-6). See Fig. 2-3 caption for legend key.

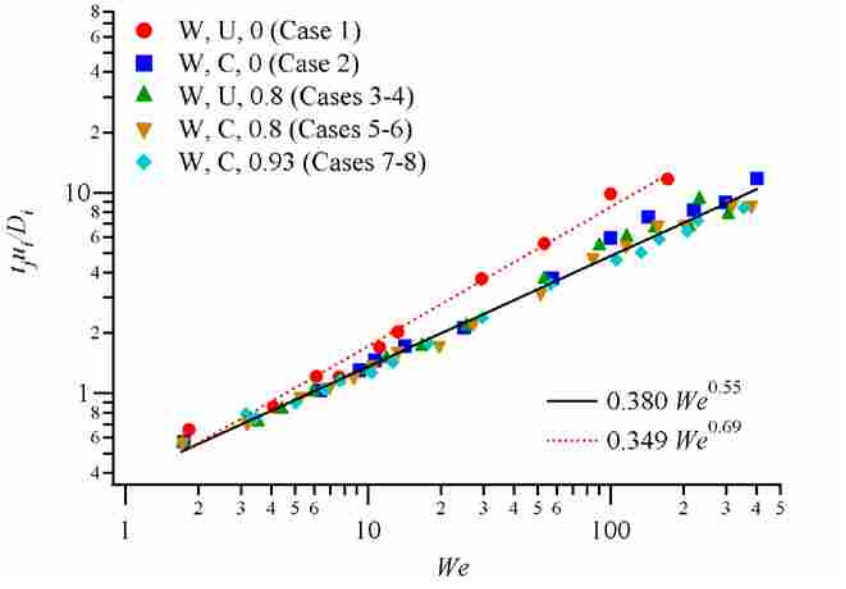

Figure 2-8: Normalized time between droplet impact and jet ejection, $t_j u_f / D_i$, as a function of *We* for water on all surfaces tested. See Fig. 2-3 caption for legend key.

suggests that the time between droplet impact and jet ejection is moderately less for surfaces with a higher contact angle or greater cavity fraction. This same behavior is observed qualitatively in the images of Fig. 2-1. For all surfaces, aside from the uncoated smooth case (Case 1), the data follow a similar trend with moderate variations at higher *We* as noted. A least-squares power-law fit through these data sets reveals the dependence $t_j u_i/D_i \sim We^{0.55}$. For the hydrophilic case (Case 1), a least-squares fit yields $t_j u_i/D_i \sim We^{0.69}$. This power-law dependence is quite similar to the *We* dependence observed with the alcohol data in Fig. 2-7. However, the magnitude of $t_j u_i/D_i$ for the alcohol data is shifted upwards by nominally a factor of 1.8.

2.4.4 Jet Velocity

The maximum normalized jet velocity is also independent of the camera viewing direction, and the results acquired in the longitudinal and transverse viewing orientations are again combined. Shown in Fig. 2-9 is the normalized jet velocity, u_j/u_i, plotted as a function of *We*. These data were acquired for a superhydrophobic surface with $F_c = 0.8$ and a fluoropolymer coating (Cases 5-6). Again, varying droplet size had no impact on the overall trends. For both the pure water and water/glycerine droplets the maximum velocity of the ejecting jet exceeds the droplet impact velocity over the range $2 \leq We \leq 150$. For the pure water data, there is a region at relatively low *We* ($5 < We < 15$) where the maximum jet velocity significantly exceeds the impact velocity, with the largest normalized jet velocities occurring at $We \approx 6$. Under certain conditions the ejecting jet velocity is observed to be as much as 15 times greater than the droplet impact velocity. In this regime, the jet that is ejected is smaller compared to the jets that exist at higher and lower *We*. Thus, by conservation principles the jet momentum forces higher speeds. This "thin jet" phenomenon was first observed by Bartolo et al. (2006). The present data also reveal that in this regime ($5 < We < 15$) there is significant variability in the dynamics. While

the micro-jet phenomena is observed more often than not, occasionally much lower jet velocities are observed, even when all other controlling factors are the same. The implication is that formation of the micro-jet is quite sensitive to small perturbations in the solid surface characteristics or droplet motion prior to impact.

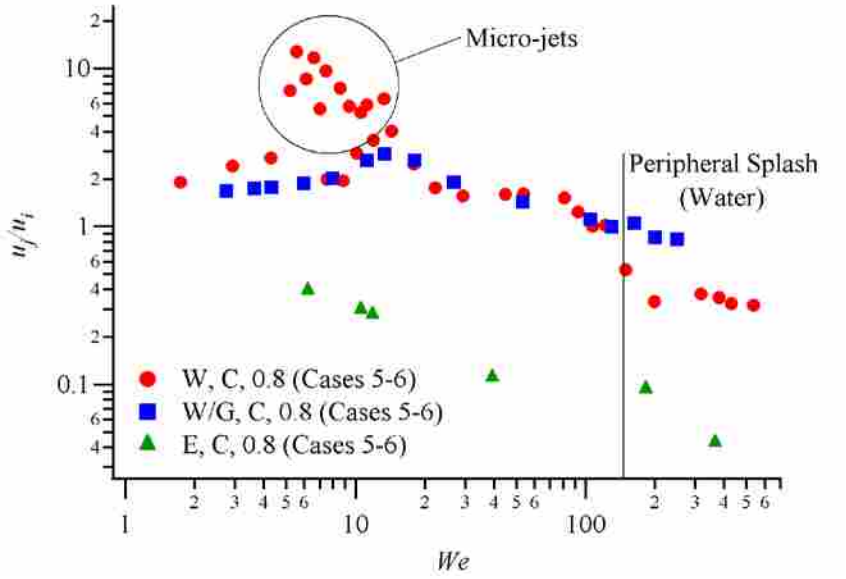

Figure 2-9: Normalized jet velocity, u_j/u_i, as a function of *We* on a superhydrophobic surface (Cases 5-6). See Fig. 2-3 caption for legend key.

For the water/glycerine mixture the micro-jet phenomenon described above is not observed, presumably due to the much greater viscosity. For this fluid type the maximum jet speed is about 3 times the droplet speed and occurs at a modestly greater Weber number than for the pure water droplets, $We \approx 14$. Further, less variability in the jet velocity is manifest for the more viscous liquid. As previously noted, the vertical velocities of the ethanol "jets" are very weak compared with those from the other fluid types, and are nominally an order of magnitude smaller. At high Weber number, $We > 150$, and for pure water droplets, the maximum normalized jet speeds are observed to be markedly weaker than at lower *We*. This decrease

coincides with the point where the spreading radial droplet is first observed to form peripheral satellite droplets. The detachment of droplets decreases the average inward radial pull and results in weaker jets due to the momentum lost to the satellite droplets. The high viscosity water/glycerine mixture was not observed to splash horizontally for the range of *We* tested, and the normalized jet velocity does not exhibit the same drop off as it did in the case of pure water at high *We*.

Figure 2-10 provides a comparison of the normalized jet velocity as a function of *We* for all surface types explored with water as the working fluid. Here it is seen that all of the surfaces that yield a contact angle in the hydrophobic range demonstrate the micro-jet phenomenon with the behavior generally following the trend described above. At $We \leq 5$, the issuing jet velocity is similar for all surfaces, including the uncoated and smooth hydrophilic surface (Case 1). However, at *We* greater than this the data for the hydrophilic case shows marked deviation, with the jet being significantly weaker over the rest of the *We* range explored. In the $5 \leq We \leq 15$

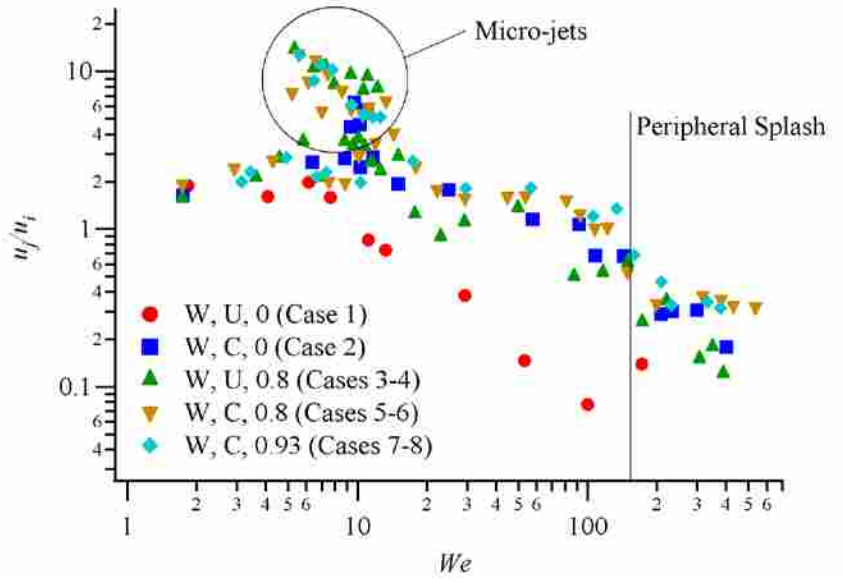

Figure 2-10: Normalized jet velocity, u_f/u_i, as a function of *We* for water on all surfaces tested. See Fig. 2-3 caption for legend key.

range significant variability is again observed for Cases 2-8. In general, in this range the jet velocities for all experiments performed on superhydrophobic surfaces (Cases 5-8) are higher than those for the hydrophobic surface (Case 2). Surprisingly, the issuing jets associated with Cases 3 and 4 (structured but uncoated surfaces) exhibit similar velocities to the superhydrophobic scenarios in the micro-jet region. However, at higher *We* the jet velocities for these surfaces tend to be lower than for the other hydrophobic surfaces (Cases 2, 5-8).

2.4.5 Other Jet Phenomena

In addition to the micro-jet behavior, there were a number of interesting unexpected phenomena that were repeatedly observed during the experiments. One of these was an early ejection of a micro-droplet prior to the main jet ejection. Figure 2-11 shows a series of images that illustrate this phenomenon. Pictured are: a) a droplet at impact (rib orientation shown), b) the droplet as it begins to spread, c) the collapsing droplet with a micro-droplet being emitted (indicated), d) the main jet ejection (indicated), and e-f) the ejected droplets moving upwards. In the case pictured the second ejection produced droplets traveling at higher speeds than the first ejection, and it can be seen that the second emission overtakes the first droplet rapidly. This early ejection was occasionally observed for water droplets in the range $9 < We < 15$, within the micro-jet region for Cases 3-8, which correspond to the cases with grooved surfaces, coated and uncoated. No explanation for this exists at present. The information obtained from the second ejection was used for the jet data of Figs. 2-7 – 2-10.

Another interesting phenomenon that was observed was the occurrence of the issuing jet splitting into two separate jets that each traveled at a slight angle from the surface normal. Images from a case where this was observed can be seen in Fig. 2-12. These images were taken

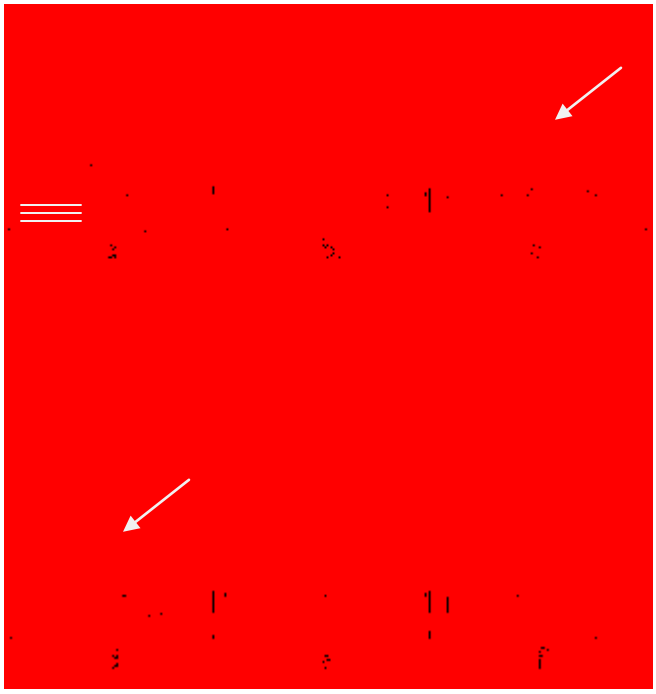

Figure 2-11: Images depicting the early ejection phenomenon. Frames show a) a droplet at impact (0 ms), b) as the droplet is spreading radially (1.8 ms), c) as a micro-droplet is ejected (3.7 ms), d) at the main ejection (6.3 ms), and e-f) as the emitted droplets continue to travel up (7 ms and 8.5 ms). Images were taken for a water droplet on a surface with F_c = 0.93 and a Teflon coating (Case 8).

using the water/glycerine mixture on a surface with F_c = 0.8, viewing the transverse spread direction, and a fluoropolymer coating (Case 5). Images show the droplet a) at impact (rib orientation also shown), b) at maximum spread diameter, c) as the droplet retracts, d) as the two-pronged jet is being ejected (indicated), e) as the jet continues to rise, and f) as the two separate jets collapse into the same jet after releasing a number of droplets. This phenomenon was only observed with water/glycerine mixture tests conducted on patterned surfaces (Cases 3-8) in the range $We > 150$. The split jet was only observable when the camera viewed the droplet motion in the transverse direction and is apparently a result of the grooves on the surface and the high viscosity of the liquid. The water/glycerine droplet tests featured one other distinction from the pure water tests. With the water tests, the ejecting jet broke into smaller droplets quite soon after

jet formation. However, in the water/glycerine tests, the ejecting jet remained intact much longer, with a tall column of liquid being formed. Again, this is an effect of the much higher liquid viscosity.

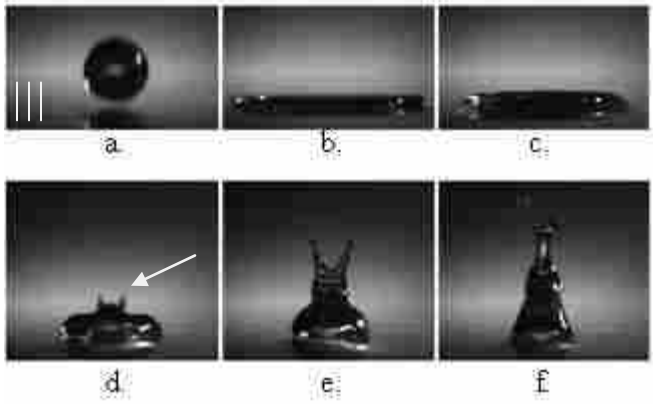

Figure 2-12: Images depicting the ejection of a split jet. Frames show a) a droplet at impact (0 ms), b) as it reaches maximum spread (2.3 ms), c) as it retracts (5 ms), d) as the split jet is ejected (7.7 ms), e) as the jets continue to move upwards (8.7 ms), and f) as the jets collapse together after releasing small droplets (9.7 ms). Images were taken for a water/glycerine mixture droplet on a surface with F_c = 0.8 and a fluoropolymer coating (Case 5).

2.4.6 Summary of Observations

An overall summary of the present data is now provided. With regard to the maximum diameter spread, no appreciable difference between superhydrophobic surfaces and other hydrophobic surfaces was observed. For all of the hydrophobic cases, a power-law relationship with a *We* dependence greater than that found in literature was observed ($D_m/D_i \sim We^{0.62}$) for all the fluid types considered. However, when examining the normalized time delay between droplet impact and maximum droplet spread there is a moderate difference between superhydrophobic surfaces and other hydrophobic surfaces at high *We*. All have a power-law dependence and scale with $We^{0.4}$. The data obtained when alcohol is used, observed in the

longitudinal direction, deviate from this dependence, much as was observed when considering maximum spread diameter. When considering the time between droplet impact and jet ejection, a power-law dependence on *We* is observed. For hydrophobic cases, $t_j u_i/D_i \sim We^{0.55}$, though the superhydrophobic surfaces have a moderately smaller $t_j u_i/D_i$ than other hydrophobic cases, and for the hydrophilic cases (alcohol tests and all tests on the smooth, uncoated surface) $t_j u_i/D_i \sim We^{0.7}$. The jet velocity data reveals that micro-jets form over the range $5 < We < 12$, with water as the liquid type, and that the jet velocities for all hydrophobic cases are much greater in this range than at any other *We* explored. Furthermore, significant variability exists in the data in this range. The data for the high-viscosity water/glycerine mixture does not exhibit this behavior and the weak "jets" experienced by the alcohol droplets have velocities that are nominally one order of magnitude less than for the other fluids tested. In general the jets velocities for the superhydrophobic scenarios are higher than those for other surfaces explored. There was no dependence on droplet size observed for any of the parameters tested.

2.5 Model Comparisons

In this section of the chapter the present experimental results are compared to two models of droplet impact on hydrophobic surfaces that have appeared in the literature. These two models, by Mao et al. (1997) and Attane et al. (2007), have been shown to provide arguably the best predictions of maximum spread diameter of all models to date for the *Oh* and *We* ranges in the present data (German and Bertola, 2009), and are thus the only models considered.

2.5.1 Empirical Model by Mao et al. (1997)

Mao et al. (1997) developed an empirical model to predict maximum spread diameter. The model was made based on isothermal droplet impact on horizontal surfaces for 30° < θ < 120°, and allows for varying degrees of surface roughness. The method of applying surface roughness utilized was random, and although it resulted in some nonaxisymmetric spreading, it was indicated that the data still followed the same general trends as the smooth surfaces tested. Figure 2-13 provides a comparison of this model with data acquired in this study on a superhydrophobic surface with all three fluid types. Data acquired in both the transverse and longitudinal spreading directions (Cases 5-6) are compared to the model results where the model parameter that varies for the two directions is the contact angle. This model has been shown previously to yield better predictions than earlier empirical or semi-empirical models, and

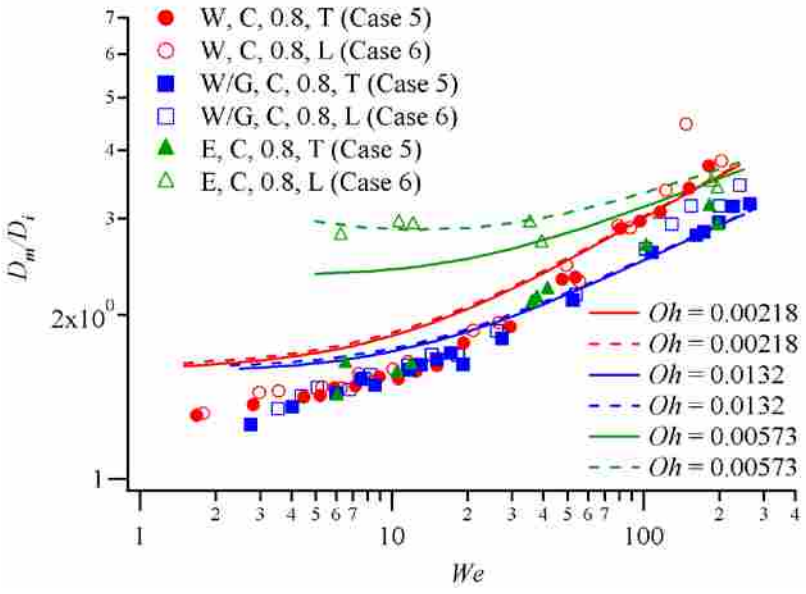

Figure 2-13: Normalized maximum droplet spread diameter, D_m/D_i, compared to the empirical prediction from Mao et al. (1997). Data for all three fluid types are represented and the data were acquired on a superhydrophobic surface with F_c = 0.8 (Cases 5-6). Solid lines represent the empirical model in the transverse direction (Case 5), and dashed lines correspond to the longitudinal direction (Case 6). See Fig. 2-3 caption for legend key.

subsequent models offer no significant improvement (Attane et al., 2007; German and Bertola, 2009). Thus, it is the only empirical model compared with the present results. The Ohnesorge number is an important parameter in the model, and values for *Oh* considered are shown on the figure. *Oh* = 0.00218, 0.0132, and 0.00573 correspond to pure water, the 50/50 water/glycerine mixture, and ethanol, respectively. It has previously been shown that this model over-predicts maximum spread diameter at lower *We* (Attane et al., 2007), and this holds true for the present data, where the model over-predicts maximum spread diameter for $We < 70$. The model, on average, exhibits an error of 14% with data from this study, although it deviates by as much as nearly 30% at low *We* for pure water and the water/glycerine mixture and nearly 70% for alcohol. At larger *We* the model and experimental results show reasonable agreement, except for the alcohol data, where the model matches the longitudinal data reasonably well, but is significantly different from the transverse data.

2.5.2 Analytical Model by Attane et al. (2007)

An analytical model was also compared with the data. Attane et al. (2007) developed a model (referred to hereafter as the AGM model) based on isothermal droplet impact on flat surfaces. This model does not take into consideration surface roughness (other than allowing the static contact angle to vary) and does not allow for surface anisotropy. It also covers the entire range of contact angle, $0° < \theta < 180°$, but does not account for apparent slip at the surface due to superhydrophobic behavior. An energy balance approach was utilized in which the droplet is modeled as a cylinder as it spreads on the surface. The AGM model considers the rimmed disk shape that exists while the droplet is spreading and retracting on the surface. This model yields better agreement with experimental data and shows good accuracy for surfaces of low to

moderate contact angle that are isotropic. This is true for the present data as well. The differential equation governing droplet radius in the AGM model is

$$\frac{1}{2}\frac{d}{d\tau}\left\{\left[\frac{2}{3}+\frac{1}{45}\frac{1}{R^6}\right]\left(\frac{dR}{d\tau}\right)^2\right\}+\frac{d}{d\tau}\left[R^2\left(1-\cos\theta\right)+\frac{1}{3R}\right]+4Oh\left[3R^4+\frac{2}{3R^2}+sR\right]\left[\frac{dR}{d\tau}\right]^2=0. \quad (2\text{-}1)$$

In the above expression s is an adjustable parameter related to dissipated power in the rim that was determined empirically to be $s = 1.41Oh^{-2/3}$. R is the droplet radius normalized by the droplet diameter at impact and θ is the static contact angle. The dimensionless time in the model, τ, is defined as $\tau = tu_i / D_i\sqrt{We}$. The initial conditions, found by equating surface energy and kinetic energy for the spreading cylinder to that of a falling sphere and the initial droplet radius and surface velocity, are expressed as:

$$1=\left[R_o^2\left(1-\cos\theta\right)+\frac{1}{3R_o}\right] \quad (2\text{-}2)$$

and

$$\left.\frac{dR}{d\tau}\right|_o=\sqrt{We}\left[\frac{2}{3}+\frac{1}{45}\frac{1}{R_o^6}\right]^{-1/2}. \quad (2\text{-}3)$$

The initial condition for R_o, the dimensionless radius at impact, only has a positive real solution for $\theta < 109.4°$, although it has been noted (Attane et al., 2007) that using a constant value for $R_o = 0.39$ for $\theta > 109°$ will give an error of less than 16% for the entire range of contact angles ($0° < \theta < 180°$).

Equation (2-1), subject to initial conditions (2-2) and (2-3) was solved numerically. Shown in Fig. 2-14 is the predicted and measured instantaneous normalized droplet diameter, D/D_i, as a function of τ for water droplets impinging on a superhydrophobic surface (Case 7). Results are shown for three values of impact *We*, and the data are compared to results from the

AGM model with the parameters in the model set to match the relevant case. The model prediction tracks the general behavior of the experimental data reasonably well. At early τ the ratio D/D_i remains near unity for the experimental data since only the bottom portion of the droplet is in contact with the surface and the spread has not yet exceeded the initial droplet diameter. The values of $D/D_i < 1$ from the model predictions represent the portion of the droplet in contact with the surface and are thus initially smaller than the impact droplet diameter. The model predictions allow extraction of the maximum spread diameter and the time delay from impact until maximum diameter is reached for each condition explored and these comparisons are made in the following sections.

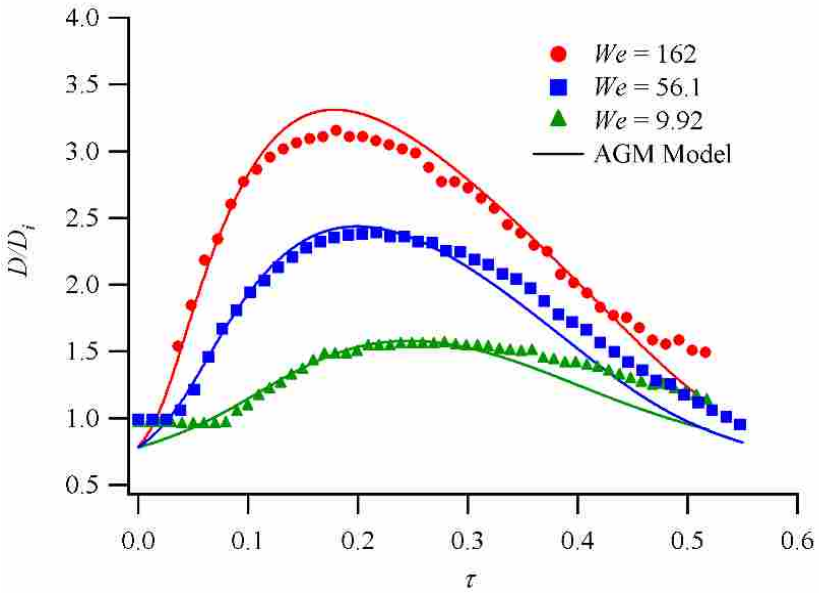

Figure 2-14: Normalized diameter, D/D_i, as a function of τ for a superhydrophobic surface with F_c = 0.93 (Case 7) and with water as the working fluid. The parameters in the model were set to match the relevant case.

Shown in Fig. 2-15 is a comparison of data derived from the present experiments and the AGM model prediction for maximum spread diameter, D_m/D_i, as a function of *We* for a

superhydrophobic scenario with F_c = 0.8. Results acquired in both the longitudinal and transverse spreading directions are shown. Values for *Oh* used in the model are listed on the figure, and are *Oh* = 0.00218 for pure water, *Oh* = 0.0132 for the water/glycerine mixture, and *Oh* = 0.00575 for alcohol. The data illustrate that the model prediction for water yields good agreement with the present experimental data for both spreading directions, but with modest deviation evident at $We \leq 5$. For the water/glycerine mixture, which corresponds to the largest *Oh* explored, the model under-predicts the maximum spread diameter by an average of 6% over the entire *We* range investigated. It is again noted that the AGM model does not account for apparent slip that prevails at the solid-liquid interface due to the superhydrophobic nature of the surface. Such slip would exert greater influence on more viscous fluids and would lead to elevated values of the maximum spread diameter due to the reduced frictional resistance.

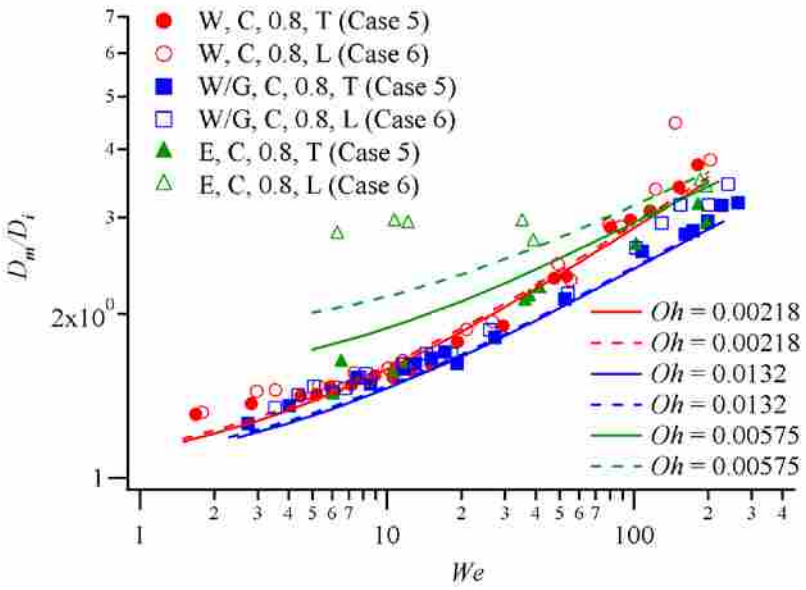

Figure 2-15: Normalized maximum spread diameter, D_m/D_i, as a function of *We* compared to results derived from the AGM model for all three fluid types and for a superhydrophobic surface with F_c = 0.8 (Cases 5-6). Solid lines correspond to the model results for the transverse direction (Case 5), and dashed lines correspond to model results for the longitudinal direction (Case 6). See Fig. 2-3 caption for legend key.

Furthermore, this effect would be more manifest in the longitudinal direction where apparent slip has been shown to be greater (Lauga and Stone, 2003; Woolford et al., 2009b). This is consistent with the high-*We* water/glycerine data where the data corresponding to the longitudinal direction shows greater deviation from the model prediction, under-predicting maximum spread diameter by 3.5% more in the longitudinal spread direction than in the transverse direction. The alcohol data show the poorest agreement with the model predictions. In this case the AGM model under-predicts the spread diameter in the longitudinal direction by 10% on average, and over-predicts the spread in the transverse direction by 15% on average. The model does predict that the spread diameters for the two directions will be different. However, the model only accounts for the change in the surface contact angle, and the existence of a grooved wetting surface is not accounted for. This is likely the reason for the error in the model prediction corresponding to the alcohol data.

Figure 2-16 shows the present data for normalized maximum diameter spread, D_m/D_i, as a function of *We* for the uncoated grooved case (Cases 3-4) compared to the corresponding AGM model prediction. The only data trends that the AGM model matches very well for this surface type are water and water/glycerine mixture tests viewed in the transverse direction. All other trends show significant deviation from the prediction, with the average error in the model in the range from 10% to 30%. The comparisons of the present data with the model derived by Attane et al. (2007) reveal that the model can be used to obtain predictions of the behavior of impacting droplets on superhydrophobic surfaces with modest error. For the present case of grooved superhydrophobic surfaces, where the contact angle only varies slightly in the major spread directions, the AGM model exhibits general agreement with the data. However, in the case of

surfaces that are more anisotropic, such as alcohol on superhydrophobic surfaces (Cases 5-8) and all fluid types on grooved, uncoated surfaces (Cases 3-4) where the surface contact angle varies significantly between the two major viewing directions, the error in the model predictions increases. It is therefore recommended that these models be used only in the case of isotropic surface conditions. Further, for liquids of relatively low viscosity where the overall frictional resistance is only modest, the models yield good agreement with the data. However, for higher viscosity fluids where apparent slip can exert greater influence, greater variation is observed. Here modifications to the existing models to account for slip at the wall are recommended.

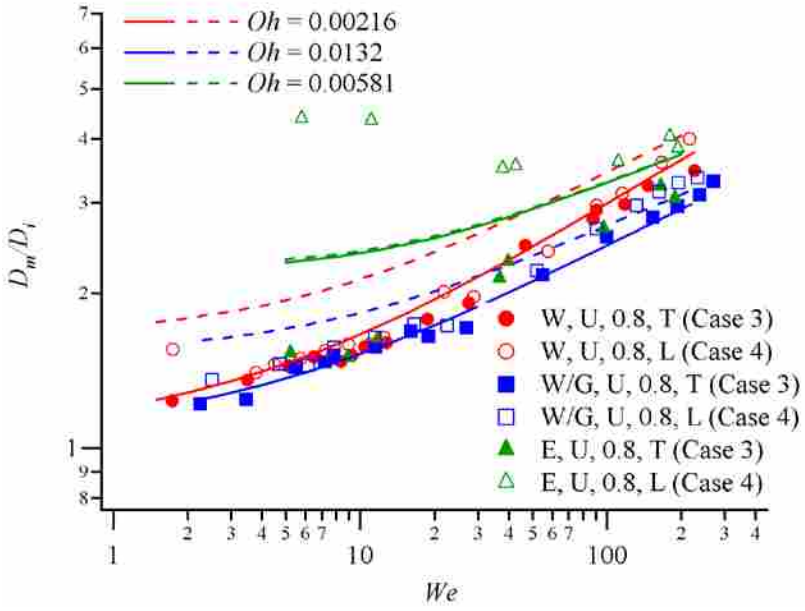

Figure 2-16: Normalized maximum spread diameter, D_m/D_i, as a function of *We* compared to results derived from the AGM model for all three fluid types and for an uncoated patterned surface with F_c = 0.8 (Cases 3-4). Solid lines correspond to the model results for the transverse direction (Case 3), and dashed lines correspond to model results for the longitudinal direction (Case 4). See Fig. 2-3 caption for legend key.

2.6 Conclusions

This paper has presented data for droplet impingement experiments performed on superhydrophobic surfaces. The fluid types used in these tests were pure water, a 50/50 water/glycerine mixture, and ethanol. For comparison, data from the following surface types were included: smooth uncoated substrates, smooth coated substrates, structured uncoated substrates, and structured coated substrates. Data were taken in the longitudinal direction (when the fluid motion was parallel to the ribs) and the transverse direction (when the fluid motion is perpendicular to the ribs). Image analysis software was used to calculate the following parameters for each experiment: Weber number, Ohnesorge number, maximum spread diameter, D_m, time between impact and maximum spread diameter, t_D, time between impact and jet ejection, t_j, and jet velocity, u_j. Data acquired covered Weber numbers ranging from 1 to 500, and Ohnesorge numbers ranging from 0.002 to 0.015. The superhydrophobic surfaces exhibited cavity fractions of 0.8 and 0.93. The data reveal only modest differences between superhydrophobic surfaces and other surfaces when considering the maximum spread diameter, though the time between impact and maximum spread diameter and the time between impact and jet ejection are modestly less for superhydrophobic surfaces than for other hydrophobic surfaces. The differences are most pronounced at higher *We* and for fluids of greater viscosity. The trends are slightly different when in the hydrophobic regime as opposed to the hydrophilic regime. Measurements of the issuing jet that forms during droplet rebound showed that in general higher jet velocities prevail for the superhydrophobic surfaces than for the other surfaces considered. A micro-jet regime was observed where water droplets were observed to have very high jet velocities, nearly 20 times the impact velocity. The data were compared to an empirical model developed by Mao et al. (1997). This model predicts maximum spread diameter, and fit

reasonably well when $We > 70$, but over-predicts maximum spread diameter for low *We*. A recent analytical model derived by Attane et al. (2007) was also compared to the experimental results and demonstrated good agreement with data taken on grooved superhydrophobic surfaces in many cases. However, the model does not account for surface anisotropy or apparent slip at the solid-liquid interface and these are two points that should be considered in model refinement.

3 QUALITATIVE OBSERVATIONS OF DROPLET IMPACT ON SUPERHYDROPHOBIC SURFACES WITH MICRO-RIBS FOR THREE FLUIDS

3.1 Abstract

Droplet impingement experiments on superhydrophobic surfaces micropatterned with micro-ribs and a hydrophobic coating were performed using three different fluid types: water, a 50/50 water/glycerine mixture, and ethanol. For comparison, the following surface types were also tested: micropatterned uncoated, smooth coated, and smooth uncoated. The experiments showed that instabilities resulting in fingering are surface and fluid dependent, although not dependent upon contact angle. The onset of peripheral splashing was generally observed to occur at a lower Weber number as the static contact angle increased. For surfaces with rib and cavity features, the droplet spread and retraction were observed to be asymmetric. For the micropatterned uncoated surfaces, a larger area of fluid penetration into the cavities was observed than for the micropatterned coated (superhydrophobic) surfaces for water and the water/glycerine mixture. Also, the liquid was observed to be pulled out of the cavities during retraction for the coated cases. For ethanol, the cavities were penetrated at all points of contact and remained so; capillary forces then caused the fluid to continue spreading along the cavities if there was no hydrophobic coating applied. The occurrence of two-pronged and oscillating jets for water/glycerine tests was observed during droplet retraction when the surface was micropatterned. The oscillating and splitting jets were stronger for the superhydrophobic surfaces than on the surfaces with patterning but no hydrophobic coating. Micro-jets with very

high velocities were observed for water, and smaller diameter jets were observed with the water/glycerine mixture in certain ranges of *We*, depending on the surface type. An interesting spread pattern with four liquid droplets clustered at about 30° from the perpendicular direction was observed for $We > 150$.

3.2 Introduction

Much recent attention has been given to the study of superhydrophobic surfaces due to their unusually strong ability to repel water. When the static contact angle of a fluid droplet deposited on a surface exceeds $\theta = 120^{o}$ then the surface can be classified as superhydrophobic. This water repelling effect is created by a combination of a hydrophobic surface chemistry and surface micro-roughness. Some of the forms of surface micro-roughness used are posts, carbon nanotube arrays, ribs, etc. (Rothstein, 2010). When fluids with a low surface tension, such as alcohols, are used on most superhydrophobic surfaces the contact angles no longer exceed 120^{o}. One group, however, has developed surfaces that maintain high contact angles even for fluids with very low surface tensions (Tuteja et al., 2008).

A previous study has shown that significantly less frictional resistance is experienced for droplets moving across superhydrophobic surfaces compared to other surface types (Yeomans and Kusumaatmaja, 2007). Utilizing superhydrophobic surfaces in continuous channel flows has yielded interesting results. Both analytical and experimental work in small channels have shown significant drag reductions in the laminar regime (Lauga and Stone, 2003; Ou et al., 2004; Ou and Rothstein, 2005; Maynes et al., 2007; Davies et al., 2006; Lee et al., 2008; Byun et al., 2008; Woolford et al., 2009a). Continuous turbulent flow over superhydrophobic surfaces is a topic of

current investigation, and results to date show varying degrees of drag reduction (Woolford, 2009b; Min and Kim, 2004; Fukagata and Kasagi, 2006; Martell et al., 2009; Jeffs et al., 2010).

Droplet impingement on superhydrophobic surfaces is another area of current interest. When a droplet impacts a superhydrophobic surface, it spreads radially along the surface in a thin sheet until the diameter reaches a maximum. Surface tension forces then cause the droplet to collapse inwards on itself with a jet issuing vertically from the center of the droplet. The droplet may bounce, completely detaching from the surface. There are many areas where this research is relevant. Liquid droplet impact has application in ink jet printing, spray cooling processes, spray coating, self-cleaning surfaces, and reduction of droplet erosion, moisture-induced efficiency losses in steam turbines, and ice formation on external surfaces of wind turbines and aircraft (Yarin, 2006; Deng et al., 2009).

Previous investigations have shown that the elapsed time that a droplet is in contact with the surface, between impact and rebound, is not a function of droplet impact velocity, but does vary with droplet diameter (Richard et al., 2002). Studies have shown that the normalized maximum spread diameter for droplets impacting superhydrophobic surfaces scales as $We^{1/4}$ (Okumura et al., 2003; Clanet et al., 2004) where $We = \rho u_i^2 D_i/\sigma$ is the droplet impact Weber number, u_i is the droplet vertical impact velocity, D_i is the droplet diameter at impact, ρ is the fluid density, and σ is the fluid surface tension. The previous chapter presented an improvement upon this relationship. Empirical models predicting maximum spread diameter have also been developed (Mao et al., 1997; German and Bertola, 2009). An analogy between bouncing behavior and spring behavior has yielded an analytical model predicting maximal deformation and contact time of the droplet (Okumura et al., 2003). Numerical simulations of droplets

impacting superhydrophobic surfaces have demonstrated excellent agreement with experimental data (Renardy et al., 2003; Pasandideh-Fard et al., 1996; Bussmann et al., 2000).

It has been shown that depending on conditions, different outcomes are possible for a droplet impacting a superhydrophobic surface. The droplet may adhere to the surface, partially bounce, or fully bounce. Also, the impacting droplet may splash peripherally. Several groups have researched the primary factors that influence transition between different impact regimes (Deng et al., 2009; Bartolo et al., 2006; Reyssat et al., 2006; Wang et al., 2007; Jung and Bhushan, 2007; Rioboo et al., 2008; Jung and Bhushan, 2008; Brunet et al., 2008; Hyväluoma and Timonen, 2009; Jung and Bhushan, 2009; Rioboo et al., 2001). One study made a comparison between electrowetting and droplet impact tests and reported a correlation in transition requirements related to the micro-structuring (Brunet et al., 2008). It has also been shown that when a droplet recedes from the surface, a liquid film on the surface may remain. This film was shown to affect the contact angle hysteresis and the contact time with the surface (Li et al., 2009).

The most common forms of surface roughness utilized in droplet impingement experiments are arrays of posts (Reyssat et al., 2006; Jung and Bhushan, 2007; Jung and Bhushan, 2008; Li et al., 2009; Kannan and Sivakumar, 2008) and randomly generated surface roughness elements (Clanet et al., 2004; Mao et al., 1997; Renardy et al., 2003; Wang et al., 2007; Rioboo et al., 2008; Jung and Bhushan, 2008; Brunet et al., 2008; Lau et al., 2003). These types of micro-roughness result in surfaces that are isotropic. The study of surfaces that exhibit anisotropy has been much more infrequent. One research group has reported that impacting droplets on a surface with alternating ribs and cavities responds differently depending on whether the fluid is moving parallel to the ribs or transverse to the ribs (Kannan and Sivakumar,

2008a; Kannan and Sivakumar, 2008b). These studies, however, were performed on surfaces that had a contact angle much less than the 120^{o} required to be classified as superhydrophobic in one or both of the major viewing directions (parallel to the ribs and perpendicular to the ribs). The previous chapter of this thesis describes droplet impact on superhydrophobic surfaces comprised of ribs and cavities. In it, experimental data quantifying the impact dynamics were presented, namely, maximum spread diameter, vertical jet velocity, time elapsed between impact and when maximum spread diameter is reached, and time elapsed between impact and emission of a vertical jet. The previous chapter served to gain a more fundamental understanding about droplet impact experiments on anisotropic surfaces. Further, there were three fluid types used in the experiments, so the effect of varying fluid properties was also explored. The experiments, however, revealed many interesting qualitative phenomena that were not fully described. The present chapter will serve to compliment the previous one in terms of observations regarding behavior that are less quantifiable.

Some few papers have previously reported qualitative observations regarding droplet impact on superhydrophobic surfaces. It has been reported that under certain conditions a small air bubble can be trapped under the center of the impacting droplet, and that fluid penetration into the surface micro-roughness is associated with the droplet being pinned to the surface (Reyssat et al., 2006). Further, qualitative factors that affect transition between different impact regimes have also been described (Rioboo et al., 2001). The qualitative effects of surface temperature on droplet impact experiments have also been described (Li et al., 2008). A ridged structure is sometimes observed immediately following impact before the droplet flattens on a surface (Renardy et al., 2003). Qualitative observations from droplet impact on a surface comprised of ribs and cavities have been described (Kannan and Sivakumar, 2008b) although

these experiments were performed on a surface that had wider ribs and cavities such that liquid always penetrated the surface roughness. Furthermore, papers discussing qualitative observations have utilized essentially only water. The purposes of this chapter are to qualitatively explore the influence of liquid type and the effect of anisotropic surfaces on liquid droplet impact on superhydrophobic surfaces.

The scope of this paper is limited to droplet impact tests on horizontal surfaces. The following surface types were tested: smooth surfaces with and without a hydrophobic coating, and micro-structured surfaces with and without a hydrophobic coating. The micro-roughness used was alternating ribs and cavities. Three fluid types were considered: pure water, ethyl alcohol, and a mixture of 50% glycerine and 50% water (based on mass). The observations that are discussed in this paper include instabilities during droplet spread and retraction. Also, the influence of fluid type and surface anisotropy on spread and retraction and the issuing jet will be discussed. The results will be discussed following a description of the experimental approach.

3.3 Method

Experiments were performed in order to explore droplet impingement on horizontal superhydrophobic surfaces. The experimental setup consisted of a hypodermic needle that could be adjusted up or down to allow for variable impact velocity. The droplets were nominally 2.5 mm in diameter for pure water and for the water/glycerine mixture, and 2 mm for alcohol. The released droplet impacted a horizontal test surface positioned below the needle. The process was illuminated with LED lighting and recorded with a high-speed camera. A high frame rate (6000 frames per second) was utilized in order to capture the transient physics during the impingement process. For each case, the Weber number associated with the droplet impact was calculated,

$We = \rho u_i^2 D_i / \sigma$ where ρ is the fluid density, u_i is the droplet impact velocity, D_i is the droplet diameter at impact, and σ is the fluid surface tension. The impact process was recorded from either a side view or a top view, looking down on the droplet from above. For side view imaging, *We* was directly calculated since D_i could be measured from the acquired images and u_i could be calculated from other measurements. In the case of top view imaging, only D_i could be measured directly, and u_i was estimated based on the height from which the droplet was released. Thus, *We* values for experiments using the top view are approximate. Data acquired covered droplet impact Weber numbers ranging from 1 to 500.

Three different fluids were utilized in the experiments: pure water (distilled), a 50/50 water/glycerine mixture, and ethyl alcohol. The alcohol has a similar viscosity to water, but with a much lower surface tension, while the water/glycerine mixture has a similar surface tension to water but with a much higher viscosity. The fluid density, viscosity, and surface tension values for the three fluid types are shown in Table 3-1.

Table 3-1: Density, viscosity, and surface tension for the three fluid types employed in the experiments.

Fluid Type	Density, ρ (kg/m^3)	Viscosity, μ (mPa·s)	Surface Tension, σ (mN/m)
Water (Munson et al., 2006)	998	0.959	72.7
50% Glycerine 50% Water (Incropera et al., 2006)	1126	5.9	69.2
Ethyl Alcohol (Deng et al., 2007)	789	1.19	22.8

As previously noted, the structured surfaces had a micro-roughness in the form of alternating ribs and cavities. These structures were fabricated using standard photolithography and etching processes (Woolford et al., 2009b). An example of the structured surfaces utilized can be seen in Fig. 3-1. Here w_c is the width of a rib and w is the combined rib and cavity width. The rib spacing is quantified by the cavity fraction, F_c, defined as $F_c = w_c/w$. Two values of F_c

were considered in this work, 0.8 and 0.93. For the surface with F_c = 0.8, w_c = 32 μm and w = 40 μm. For the surface with F_c = 0.93, w_c = 37.25 μm and again w = 40 μm. For both cases the ribs are 15 μm high. For the purposes of the droplet impact experiments the ribs are considered to be infinitely long, since the liquid never reaches the edges of the ribs during the impingement process.

Figure 3-1: An SEM image of the rib and cavity structures used in the experiments. Labeled on the image are the width of a cavity, w_c, and the combined rib and cavity width, w.

Because of the anisotropy in the frictional resistance, and in the droplet contact angles created by the rib and cavity features, the droplet impingement tests were imaged from the two normal directions: when the fluid moves parallel to the ribs (the longitudinal direction), and perpendicular to the ribs (the transverse direction). For all surfaces and liquid types the liquid-solid static contact angle was measured using a goniometer for both the longitudinal (L) and transverse (T) orientations. The static contact angles, averaged over ten measurements, for all surface and fluid types employed in the study are shown in Table 3-2.

Table 3-2: Static contact angles in the transverse (T) and longitudinal (L) directions for all surface and fluid types employed in the present study.

Case #	Coating	F_c	Rib Orientation	Contact Angle, θ (º)		
				Water	Water-Glycerine Mixture	Alcohol
1	None	0	N/A	54.1	53.1	20
2	Fluoro	0	N/A	121.4	114.6	53.8
3	None	0.8	T	128.6	122	12.7
4	None	0.8	L	65	58.6	9
5	Fluoro	0.8	T	156.8	152.2	71
6	Fluoro	0.8	L	149.2	144.2	43.5
7	Teflon	0.93	T	160.7	157.8	74.8
8	Teflon	0.93	L	152.9	155.2	45

Two hydrophobic coatings were employed, a fluoropolymer (a solution of Fluoropel M1604V and MQ000 (Woolford, 2009)) and Teflon as indicated in Table 3-2. A spin-on process was used to apply these coatings (Woolford et al., 2009b). Also shown in the table is the cavity fraction, F_c. As shown by the data of Table 3-2, the contact angle is less when measured in the longitudinal direction (parallel to the ribs) than for the transverse direction. For the cases when superhydrophobic behavior prevails (Cases 5-8 in Table 3-2 with water or water/glycerine mixture), the difference in θ in the two directions is not large. However, it is significant for the uncoated structured scenarios (Cases 3-4) with either pure water or the water/glycerine mixture as the fluid type. Here θ is much greater for the transverse direction ($\theta > 120^o$) than it is for the longitudinal direction ($\theta < 70^o$). The alcohol exhibits hydrophilic contact angles ($\theta < 90^o$) for all surface types, and exhibits significant variation between the contact angles in the two directions (approximately 30°) for the coated and structured surfaces (Cases 5-8).

3.4 Results and Discussion

In this section of the chapter the observations and results obtained will be presented. First, instabilities arising during the droplet spreading on surfaces will be considered. This will be followed by non-axisymmetric spreading and retraction observations, and then interesting observed jet emission behavior will be discussed. The results for the different fluid types and surface types will be compared to the baseline case where water droplets impact a smooth surface that has a hydrophobic coating applied (Case 2).

Figures 3-2 and 3-3 show top-view images and side-view images, respectively, taken for this baseline case at three different values of *We*. The images illustrate four frames during the transient event for a) $We \approx 5$, b) $We \approx 50$, and c) $We \approx 300$. The frames show, from top to bottom, the droplet at impact (0 ms), at the maximum spread diameter (about 3.7 ms), as a vertical jet is being ejected (about 8 ms), and as the droplet is rebounding from the surface (about 18 ms). It is interesting to consider the normalized maximum spread diameter, D_m/D_i, and the normalized jet ejection velocity, u_j/u_i. In these expressions, D_m is the diameter at maximum spread, D_i is the diameter of the droplet at impact, u_j is the maximum vertical velocity of the jet, and u_i is the impact velocity. For the three *We* considered, measurements show that a) $D_m/D_i \approx 1.5$ and $u_j/u_i \approx 1.8$, b) $D_m/D_i \approx 2.4$ and $u_j/u_i \approx 1.2$, and c) $D_m/D_i \approx 4$ and $u_j/u_i \approx 0.3$. At low *We* (Fig. 3-2a and 3-3a) the droplet spreads and retracts, but always remains in contact with the surface. As *We* increases, (Fig. 3-2b and 3-3b) the droplet spreads to a much further extent, and the upward rebound motion increases in strength such that the droplet completely leaves the surface. At even higher *We* (Fig. 3-2c and 3-3c) the rim becomes unstable and breaks into fingers. This causes the ejected jet to leave the surface obliquely, with the angle of departure dependent on how the fingers form. Also, at high *We* peripheral splashing begins, in which

satellite droplets form that are released horizontally away from the impact site. At high *We* the droplet continues to rebound from the surface, despite energy losses due to fingering and satellite droplet formation.

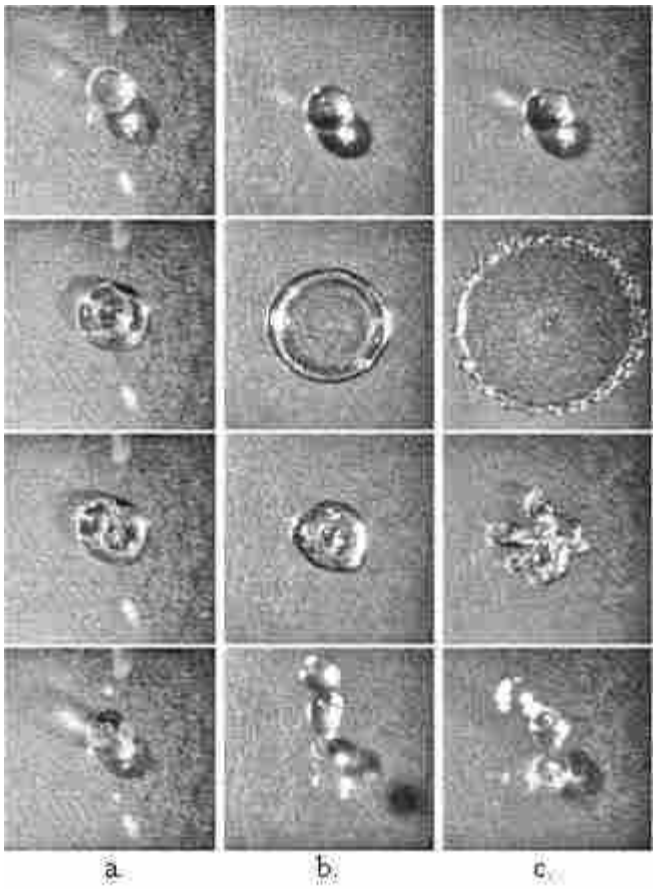

Figure 3-2: Top view images of water droplets impacting a smooth coated surface (Case 2). a) *We* ≈ 5, b) *We* ≈ 50, c) *We* ≈ 300. Frames show, from top to bottom, the droplet at impact, at maximum spread, as a vertical jet is being issued from the center, and as the droplet is rebounding from the surface.

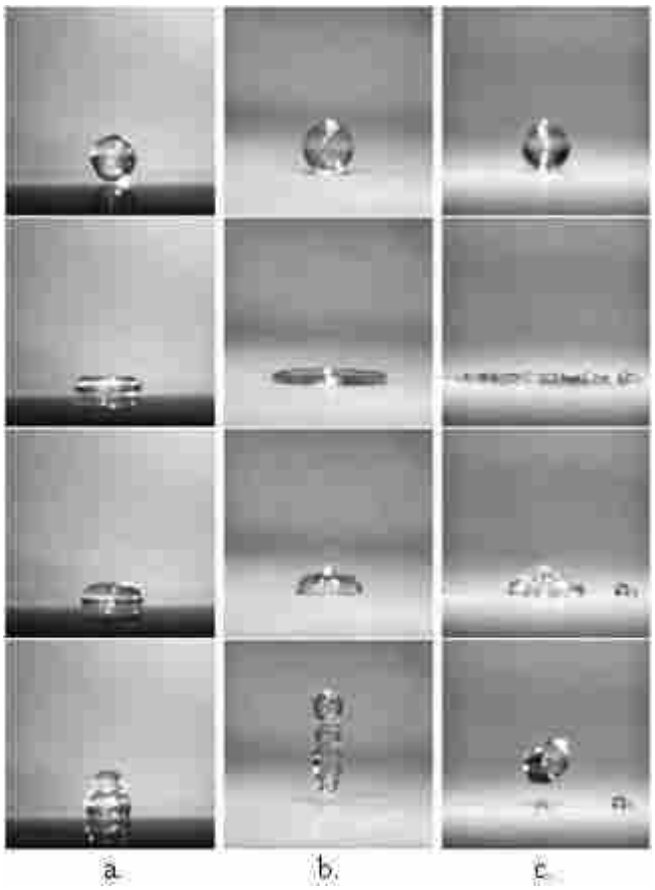

Figure 3-3: Side view images of water droplets impacting a smooth coated surface (Case 2) for a) *We* ≈ 5, b) *We* ≈ 50, and c) *We* ≈ 300. Frames show, from top to bottom, the droplet at impact, at maximum spread, as a vertical jet is being issued from the center, and as the droplet is rebounding from the surface.

3.4.1 Onset of Fingering

The value of *We* at which fingering first begins is both fluid- and surface-dependent. Fingering begins as a slight ripple around the rim during retraction, and as *We* increases, this becomes very pronounced, as observed in frame 2 of Fig. 3-2c. For pure water, fingering was observed at $We \geq 80$ for all surface types except the smooth uncoated surface (Case 1). For the smooth hydrophilic surface fingering was not observed over the entire range of *We* explored. For the water/glycerine mixture, fingering was first observed to occur between $We \approx 150$ and $We \approx 230$, depending on surface type. The specific *We* values where fingering began for each

surface type are as follows: smooth uncoated (Case 1), *We* ≈ 190; smooth coated (Case 2), *We* ≈ 150; patterned uncoated (Cases 3-4), *We* ≈ 230; and patterned coated (Cases 5-8), *We* ≈ 190. These results show that for this fluid type the hydrophobic coating causes onset of fingering at a lower *We* and the rib and cavity features delay the onset of fingering modestly. For ethanol, fingering was observed to begin in the range 140 < *We* < 200, depending on surface type, except for the smooth uncoated case (Case 1), where again fingering was not observed. For the smooth coated surface (Case 2) fingering began at *We* ≈ 200, for the patterned uncoated surface (Cases 3-4) it began at *We* ≈ 140, and for the patterned coated surfaces (Cases 5-8) it began at *We* ≈ 155. It is surprising that for ethanol the onset of fingering is at lower *We* than for the surfaces with ribs and cavities, which is opposite to the observed behavior with the water/glycerine mixture. The value of *We* at onset of fingering plotted against static contact angle can be seen in Fig. 3-4. For patterned surfaces, contact angles were averaged for the two spread directions for ease of graphical presentation. This graph shows that there is very little, if any, contact angle dependence and that when water is used, the onset of fingering is much lower than for the other surfaces.

3.4.2 Onset of Peripheral Splashing

Fluid and surface type also affected the value of *We* at which peripheral splashing was first observed. The onset occurred at lowest *We* for water where it was observed to occur between 175 < *We* < 230. Similar to fingering, splashing was not observed for the smooth uncoated surface (Case 1) over the entire range of *We* explored. For the smooth coated surface and the patterned uncoated surface (Cases 2-4), splashing was observed beginning at *We* ≈ 230. For the patterned coated surfaces (Cases 5-8), splashing was observed beginning at *We* ≈ 175. When the water/glycerine mixture was employed peripheral splashing was observed to begin at

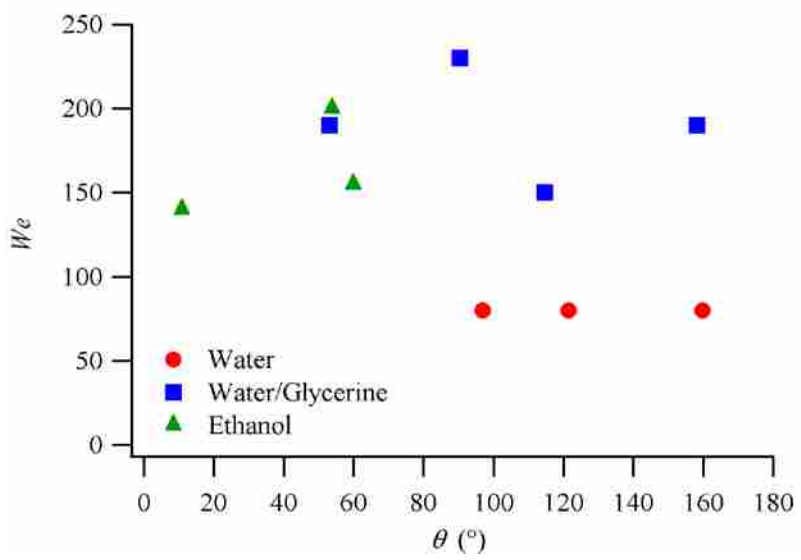

Figure 3-4: Plot of *We* at onset of fingering as a function of static contact angle. For patterned surfaces, contact angles in the two directions were averaged.

We ≈ 260 for the uncoated smooth surface (Case 1). When a coating is added (Case 2), splashing begins at *We* ≈ 275, and for the patterned coated surface (Cases 7-8) it begins at *We* ≈ 285. For the uncoated surfaces with F_c = 0.8 peripheral splashing wasn't observed over the range of *We* explored (up to *We* ≈ 350) when the water/glycerine mixture was the fluid type. When ethanol was the working fluid peripheral splashing didn't begin until *We* ≥ 330. Peripheral splashing begins at *We* ≈ 400 for the smooth uncoated case (Case 1), at *We* ≈ 450 for the patterned uncoated case (Cases 3-4), at *We* ≈ 330 for the smooth coated case (Case 2), and at *We* ≈ 250 for the patterned coated case (Cases 5-8). A graph of *We* at the onset of peripheral splash plotted against the static contact angle can be seen in Fig. 3-5. Again, the contact angles in the two spread directions are averaged for the patterned surfaces. This figure illustrates that, in general, the onset of peripheral splash occurs at a lower *We* as contact angle increases. An exception to this trend is the water/glycerine mixture, for which peripheral splash happens at a higher *We* as

contact angle increases. The cases where splashing wasn't observed are also exceptions to the general trend.

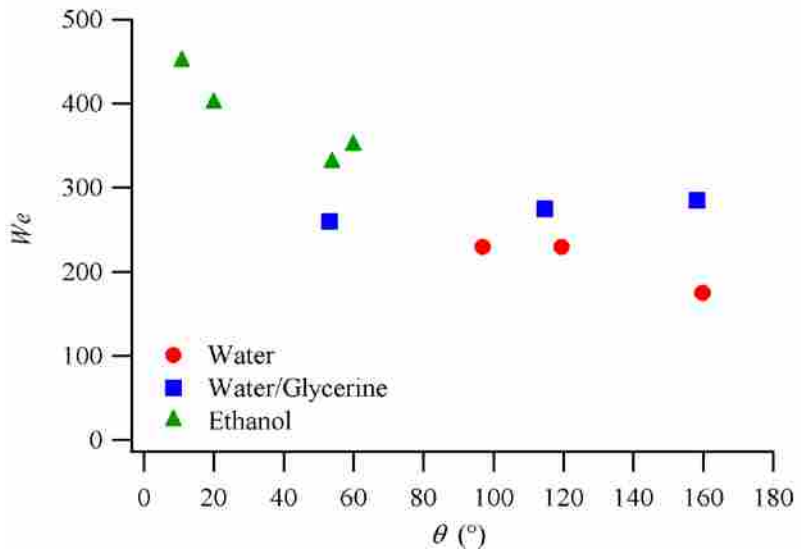

Figure 3-5: Graph of *We* at onset of peripheral splash as a function of static contact angle. For patterned surfaces, contact angles in the two directions were averaged.

3.4.3 Asymmetric Spreading/Retraction: Water on Patterned Uncoated Surfaces

The qualitative nature of the spreading and retracting of the droplet will now be discussed. On the surfaces without any surface texturing, the spreading and retracting is always axisymmetric, except when instabilities (i.e., fingering and splashing) disrupt the fluid motion. When the surfaces are patterned with ribs and cavities, the spreading and receding are asymmetric, and interesting phenomena are observed. First, the patterned surface with no coating (Cases 3-4) will be considered. For $We \leq 50$ there are no significant qualitative differences from the images seen in Fig. 3-2a. Figure 3-6 depicts water droplets impacting the uncoated patterned surface at $We \approx 50$ as viewed from a) the transverse direction (fluid moves perpendicular to the ribs, i.e., the ribs are oriented into the page), b) the longitudinal direction

(fluid moves parallel to the ribs, i.e., the ribs are oriented from side to side in the images) , and c) the top. For all top view images in this chapter where the surface is comprised of ribs and cavities, the ribs are oriented vertically on the page. Rib orientation will be noted on all image sets. The frames of Fig. 3-6 depict, from top to bottom, the droplet at impact (0 ms), as it reaches maximum spread diameter (2.9 ms), as a vertical jet is being ejected (6.8 ms), and as the droplet rebounds from the surface (12.1 ms). Also, the top frame of each shows the rib orientation. For this case, $D_m/D_i \approx 2.4$ in the transverse direction, $D_m/D_i \approx 2.5$ in the longitudinal

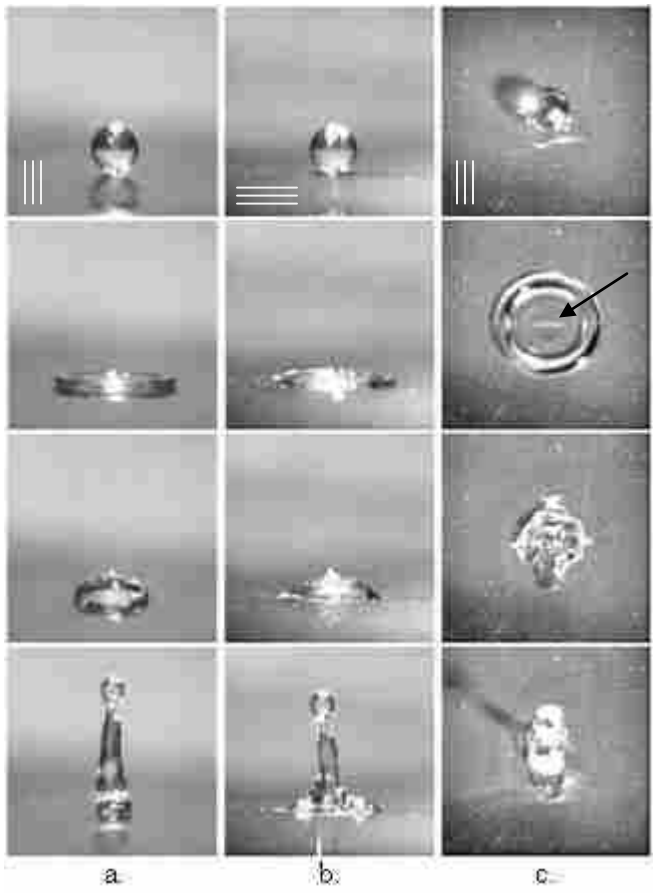

Figure 3-6: Images of water droplets impacting an uncoated surface patterned with ribs and cavities (Cases 3-4) for *We* ≈ 50. Shown are a) the transverse view, b) the longitudinal view, and c) the top view. Frames show, from top to bottom, the droplet at impact, at maximum spread diameter, as a vertical jet is ejected, and after the vertical jet has formed.

direction, and $u_j/u_i \approx 1.4$. It can be seen in the images that the droplet spreads to a thin disk and then retracts. However, here the droplet remains attached to the surface in an area that is nominally the same width (transverse direction) as the droplet diameter prior to impact and equal to the length (longitudinal direction) of the maximum spread. In the second image from the top of Fig. 3-6c a faint darker region on the surface exists and is evidence that the fluid has penetrated the cavities beneath the impact location. It can also be assumed that the fluid has penetrated the cavities from the impact site to the extent of the spread in the longitudinal direction since the fluid remains attached in that area. This is illustrated in the bottom frames of Figs. 3-6b and 3-6c. In addition, a horizontal white line at the center of the spread area (as indicated on second frame from the top of Fig. 3-6c) reveals the presence of trapped air directly under the impact location. This trapped air also spans a width nominally equal to the droplet diameter prior to impact. After the droplet has retracted, a film can be faintly seen on the surface where the fluid wetted the tops of the ribs, but didn't penetrate the cavities (bottom two frames of Fig. 3-6c).

Depicted in Fig. 3-7 are water droplets impinging upon a micropatterned uncoated surface for $We \approx 250$ from a) the transverse view, b) the longitudinal view, and c) the top view. The frames show, from top to bottom, the droplet at impact along with the rib orientation (0 ms), as it reaches maximum spread diameter (2.7 ms), as a vertical jet is being ejected (7.8 ms), and as the droplet rebounds from the surface (13.1 ms). For this case, $D_m/D_i \approx 3.2$ in the transverse direction, $D_m/D_i \approx 3.8$ in the longitudinal direction, and $u_j/u_i \approx 0.3$. It can be seen that the droplet spreads in a thin disk as before, although for this case instabilities cause significant fingering and a weak jet. Again, there is a region of cavity penetration that can be seen (indicated in second frame from the top in Fig. 3-7c), although for the high *We* case the penetrated area does not

extend to the edge of the spread area as it did for the *We* ≈ 50 case. This is illustrated in the bottom frame of Fig. 3-7c, where it is discovered that the residue left on the surface extends beyond the portion where the droplet is attached to the surface (as indicated in the longitudinal direction). In general only the cavities directly under the impacting droplet were observed to be wetted for this case.

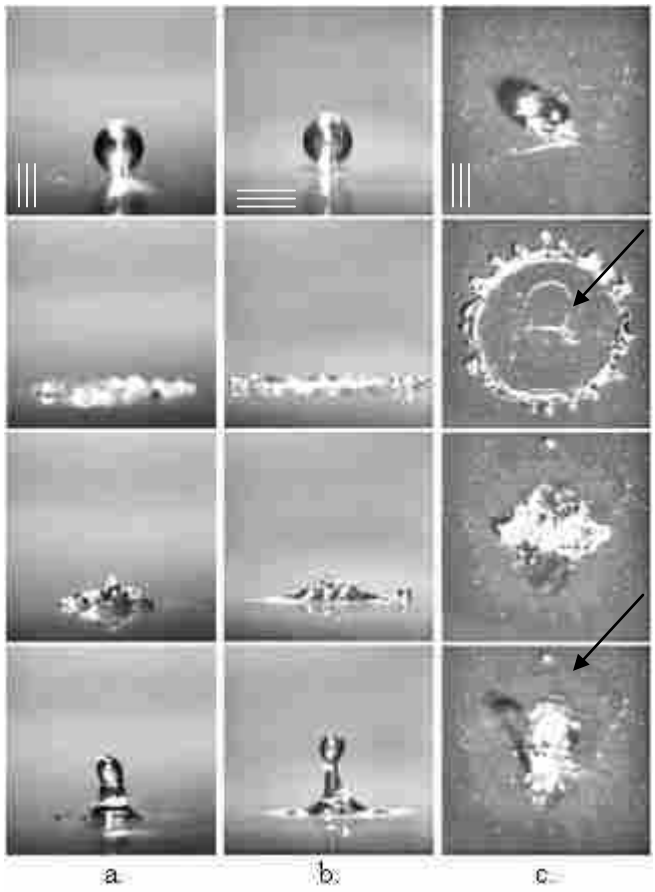

Figure 3-7: Images of water droplets impacting a patterned uncoated surface (Cases 3-4) for *We* ≈ 250. Frames depict, from top to bottom, a droplet at impact, at maximum spread diameter, as a jet is ejected, and as the jet continues to rise.

3.4.4 Water/Glycerine Mixture on Patterned Uncoated Surfaces

For experiments using the water/glycerine mixture on the uncoated patterned surface (Cases 3-4) similar behavior is observed to that when pure water is used. For the case when $We \approx 50$, there are no significant qualitative differences from the behavior of Fig. 3-6. For the case when $We \approx 250$, however, there are significant differences. The main difference is that for the water/glycerine mixture, the high viscosity of the fluid has caused the peripheral splashing and stronger fingering to be delayed. Consequently, there is still a relatively stable collapse and jet ejection at $We \approx 250$. Figure 3-8 shows the water/glycerine mixture impacting the uncoated patterned surface (Cases 3-4) for $We \approx 250$. Three viewing directions are shown: a) the transverse view, b) the longitudinal view, and c) the top view. The frames show, from top to bottom, the droplet at impact (0 ms), at maximum spread diameter (2.6 ms), as a jet is being ejected (8.5 ms), and as the jet continues to rise in the final two frames (10.4 ms and 16 ms). For this case, $D_m/D_i \approx 3.1$ in the transverse direction, $D_m/D_i \approx 3.2$ in the longitudinal direction, and $u_j/u_i \approx 0.6$. These values demonstrate another effect of the high viscosity. The spreading droplet is much more stable at this high *We*. Thus the normalized maximum spread diameter is approximately the same in the two directions, and the jet velocity is about twice as strong as for water at this value of *We*. Again, the top view reveals an area where the cavities have been penetrated by the liquid (indicated on second frame in Fig. 3-8c). This area is of comparable size to the area wetted by water for the same surface and at the same *We*. Similar to experiments where water is the test fluid, there is a residue left on the ribs, as can be seen in the bottom three frames of Fig. 3-8c.

The side views of the impact reveal interesting behavior in the jet ejection. As indicated in the third frame of Fig. 3-8a it can be seen that the jet, instead of being a single circular

ejection, is initially two-pronged. This phenomenon is only observed when the water/glycerine mixture is used and in the transverse view. This phenomenon will be discussed in more detail later. In connection with the two-pronged jet ejection, it is also observed that the jet exhibits oscillations as it rises. Both of these phenomena are consequences of the asymmetric retraction.

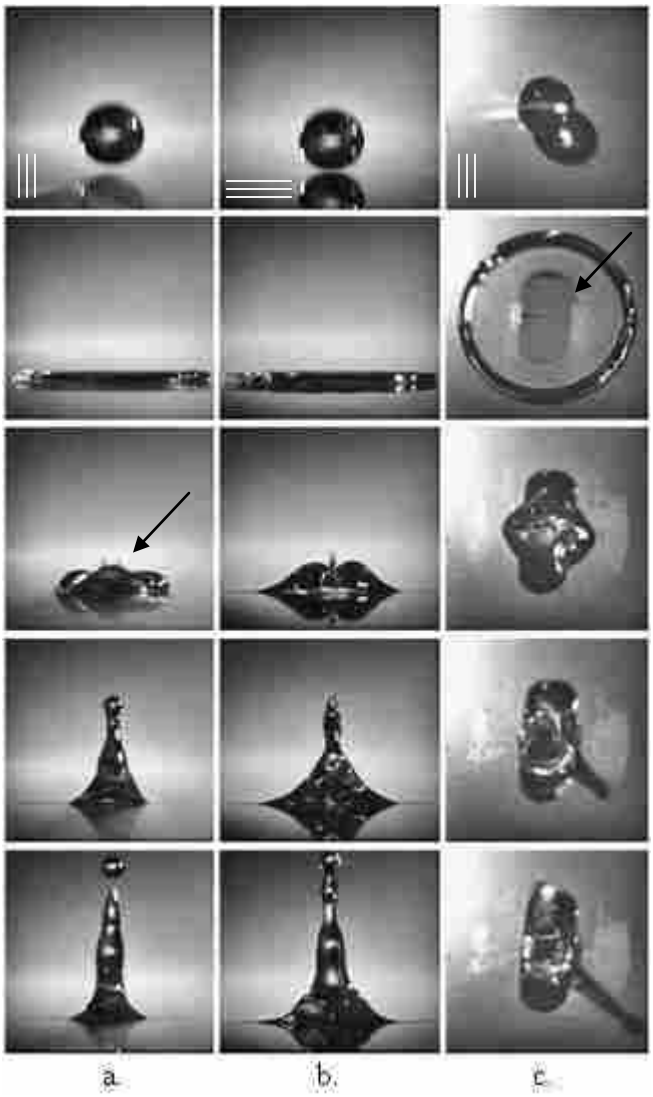

Figure 3-8: Images depicting the impact process for a droplet composed of the water/glycerine mixture impacting the uncoated patterned surface (Cases 3-4) for *We* ≈ 250. Images are taken from a) the transverse view, b) the longitudinal view, and c) the top view. The frames show, from top to bottom, the droplet at impact, at maximum spread diameter, as a jet is being ejected, and the final two images show the jet motion.

The fluid retracts moderately faster in the longitudinal direction since there is greater slip in this direction, whereas in the transverse direction the apparent slip is smaller. The two-pronged and oscillating jet are not observed when water is the working fluid; this is attributed to instabilities at this range of *We* caused by the earlier onset of the peripheral splash. The oscillation is observed for $We > 50$ over the entire range of *We* tested.

3.4.5 Ethanol on Patterned Uncoated Surfaces

Experimental results for surfaces with ribs and cavities but no coating were much different when ethanol was used as the working fluid. An ethanol droplet impacting this surface is shown in Fig. 3-9 for $We \approx 50$ for a) the transverse view, b) the longitudinal view, and c) the top view and $We \approx 250$ for d) the top view. The frames in the figure show, from top to bottom, the droplet at impact (0 ms), as it reaches maximum spread in the transverse direction (4 ms for a-c and 2.8 ms for d), as it reaches maximum inertial spread in the longitudinal direction (10.2 ms for a-c and 6 ms for d), and as it approaches equilibrium (27 ms for a-c and 77 ms for d). For the low *We* case (Fig. 3-9a-c), $D_m/D_i \approx 2.2$ in the transverse direction, $D_m/D_i \approx 3.6$ in the longitudinal direction, and $u_j/u_i < 0.1$. For the high *We* case (Fig. 3-9d), $D_m/D_i \approx 3.3$ in the transverse direction, $D_m/D_i \approx 3.9$ in the longitudinal direction, and $u_j/u_i < 0.1$. For ethanol tests on this surface, the vertical jet is essentially absent. It can be seen in the figure that the spread is more circular for the high *We* case (Fig. 3-9d), although both eventually form a rectangle with rounded corners. Also, the images in Fig. 3-9b show that the rim formed upon spreading is becoming unstable for the high *We* case. The fingering that is seen only occurs in the fluid moving in the transverse direction, while the fluid moving in the longitudinal direction remains essentially smooth.

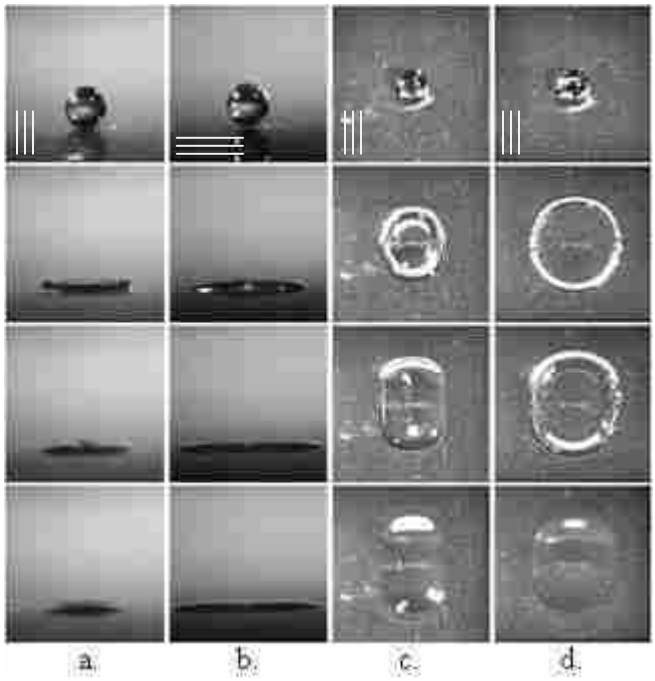

Figure 3-9: Images of ethanol droplets impacting an uncoated patterned surface (Cases 3-4) for *We* ≈ 50 from a) the transverse view, b) the longitudinal view, and c) the top view and *We* ≈ 250 from d) the top view. Images show, from top to bottom, a droplet at impact, at maximum spread in the transverse direction, at maximum inertial spread in the longitudinal direction, and as it approaches equilibrium.

For both values of *We* shown in Fig. 3-9, there is a period of inertial spreading which is followed by spreading due to capillary forces along the ribs. This wicking along the ribs continues until the fluid evaporates. Because of this continued spreading, there isn't a strong retraction in the longitudinal direction for this case. This spreading due to capillary forces is not surprising, due to the very small contact angles involved (12.7° in the transverse direction and 9° in the longitudinal direction, as seen for Cases 3-4 in Table 3-2). It was shown in the previous chapter that the maximum spread in the transverse direction is similar to that of the other fluid types on this surface, while the spread in the longitudinal direction is much more than other fluid types for *We* < 100. A close inspection of the full image sets show that in this lower range of *We* the fluid retracting in the transverse direction causes acceleration in the spread in the longitudinal

direction. As *We* increases this effect diminishes, and for *We* > 100 the retraction in the transverse direction no longer appears to cause the spread in the longitudinal direction to accelerate, even though the fluid continues to exhibit greater spread in the longitudinal direction.

3.4.6 Water on Patterned Coated Surfaces

When a coating is added to the surface patterned with ribs and cavities (Cases 5-8), the impact dynamics are notably altered. For the surfaces with micro-patterning and a hydrophobic coating, the contact angles for water and the water/glycerine mixture are in the superhydrophobic regime. Figure 3-10 shows a water droplet impacting a superhydrophobic surface (Cases 7-8) for *We* ≈ 50 from a) the transverse view, b) the longitudinal view, and c) the top view and *We* ≈ 250 for d) the top view. From top to bottom, the frames show a droplet at impact (0 ms), at maximum spread (2.7 ms for a-c and 2.5 ms for d), as a vertical jet is formed (6.3 ms for a-c and 7 ms for d), and as the droplet is rebounding from the surface (9 ms for a-c and 17 ms for d). For the low *We* case (Fig. 3-10a-c), $D_m/D_i \approx 2.5$ in the transverse direction, $D_m/D_i \approx 2.7$ in the longitudinal direction, and $u_j/u_i \approx 1.8$. For the high *We* case (Fig. 3-10d), $D_m/D_i \approx 4$ in the transverse direction, $D_m/D_i \approx 4.5$ in the longitudinal direction, and $u_j/u_i \approx 0.4$. A comparison of Fig. 3-10a and Fig. 3-10b reveals that there is very little qualitative difference in the jet viewed in the longitudinal and transverse directions at low *We*. The side view images for the high *We* case are not included, since the droplets released peripherally significantly disturb the images. As indicated in the second frame from the top in Fig. 3-10c and 3-10d it can be seen that again, the cavities are penetrated at the impact site. However, unlike for the uncoated case, the region of penetrated cavities is confined to the area just beneath the impacting droplet and extends only a very small distance along the ribs. Reyssat et al. (2006) also observed fluid penetrating the surface texture of superhydrophobic surfaces in droplet impact tests, except in their experiments

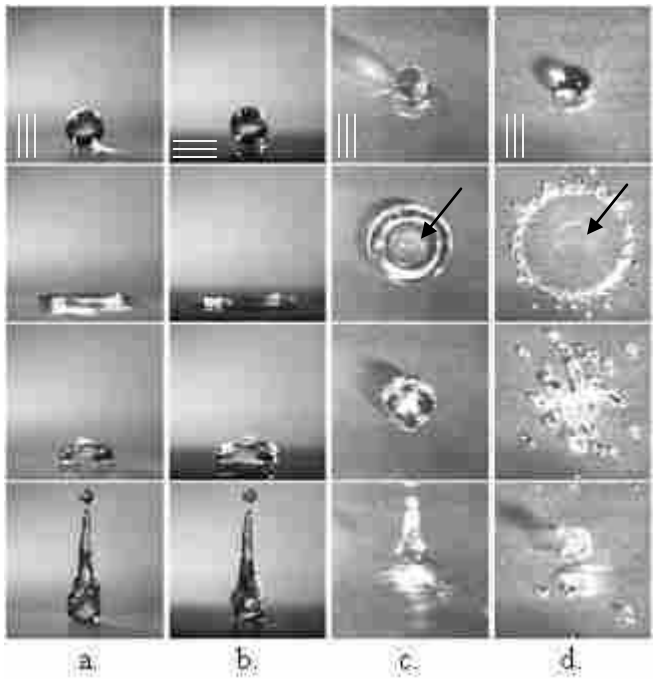

Figure 3-10: Images showing the impact process for water droplets impinging upon a superhydrophobic surface (Cases 7-8) for *We* ≈ 50 from a) the transverse view, b) the longitudinal view, and c) the top view and *We* ≈ 250 for d) the top view. From top to bottom, the frames show the droplet at impact, at maximum spread, as a jet is ejected, and as it is rebounding from the surface.

the surface roughness was in the form of posts instead of ribs and cavities. They observed a nearly square region where the fluid penetrated the posts, whereas the present data show a region of penetration that is oval in shape.

Another difference between the superhydrophobic case and the uncoated patterned case is that the fluid is all pulled out of the cavities during retraction. The third frame from the top in Fig. 3-10c reveals that the retraction isn't completely axisymmetric, and it appears that the retraction is slowest along the major axes. The higher *We* set (Fig. 3-10d) is affected strongly by the peripheral splash that happens. A large number of satellite droplets form at the sides of the liquid ring which then propagate outward from the impact location. Several droplets are also

pinched off as the fingers form and retract. The main portion of the droplet still rebounds from the surface, in spite of the lost momentum and the instabilities due to the peripheral splash.

3.4.7 Water/Glycerine Mixture on Patterned Coated Surfaces

The experiments conducted with the water/glycerine mixture on the superhydrophobic surface showed some similarities with those using water, with the most significant differences at high *We*. Shown in Fig. 3-11 is a comparison of impinging droplets of the water/glycerine mixture on a superhydrophobic surface (Cases 7-8) at $We \approx 50$ from a) the transverse view, and b) the top view, and $We \approx 250$ from c) the transverse view, and d) the top view. The frames in Fig. 3-11 show, from top to bottom, the droplet at impact (0 ms), at maximum spread (3.3 ms for a-b and 2.4 for c-d), as a jet is being ejected (7.2 ms for a-b 7.6 ms for c-d), and as it rebounds from the surface (12 ms). As indicated in the second frame from the top in Figs. 3-11b and 3-11d, there is again an oval section where the cavities have been penetrated by the fluid beneath the impact site. The retraction is modestly faster in the longitudinal direction than the transverse direction, which again causes the splitting and oscillating jets. The jet can be observed to be two-pronged as indicated in the third frame from the top in Fig. 3-11c. The oscillation is again observed for $We > 50$ over the entire range of *We* tested. The droplet doesn't leave the surface entirely, as can be seen in the final frame of Figs. 3-11b and 3-11d where a very small droplet can be seen attached to the surface after the bulk of the fluid has detached. The most notable difference between pure water and the water/glycerine mixture is seen in the $We \approx 250$ cases. The water has a strong peripheral splash at this value of *We*, while the water/glycerine mixture does not, although fingering is prevalent.

Figure 3-11: Images of droplets of the water/glycerine mixture impinging upon a coated structured surface (Cases 7-8) at *We* ≈ 50 from a) the transverse view and b) the top view and *We* ≈ 250 from c) the transverse view and d) the top view. Frames show, from top to bottom, the droplet at impact, at maximum spread, as a vertical jet is being issued, and as it is rebounding from the surface.

A close inspection of the full image sets reveals that the oscillations in the jet at high *We* are somewhat stronger on the superhydrophobic surface than on the patterned but uncoated surface (Cases 3-4). As noted in the discussion of Fig. 3-8, for the uncoated case, the two prongs that initially form rapidly coalesce. However, for the coated patterned surfaces, the two prongs remain separate much longer, and are even observed to release upward-moving droplets simultaneously. This phenomenon has not been reported in previous literature. Figure 3-12 illustrates this phenomenon for a) the patterned but uncoated surface (Cases 3-4) and b) a patterned coated surface (Cases 7-8) as a function of *We*. The values of *We* shown in Fig. 3-12a are, from top to bottom, 220, 250, 290, and 330. For Fig. 3-12b, the *We* values are, from top to bottom, 195, 205, 250, and 270. The two-pronged phenomenon is very consistent within these

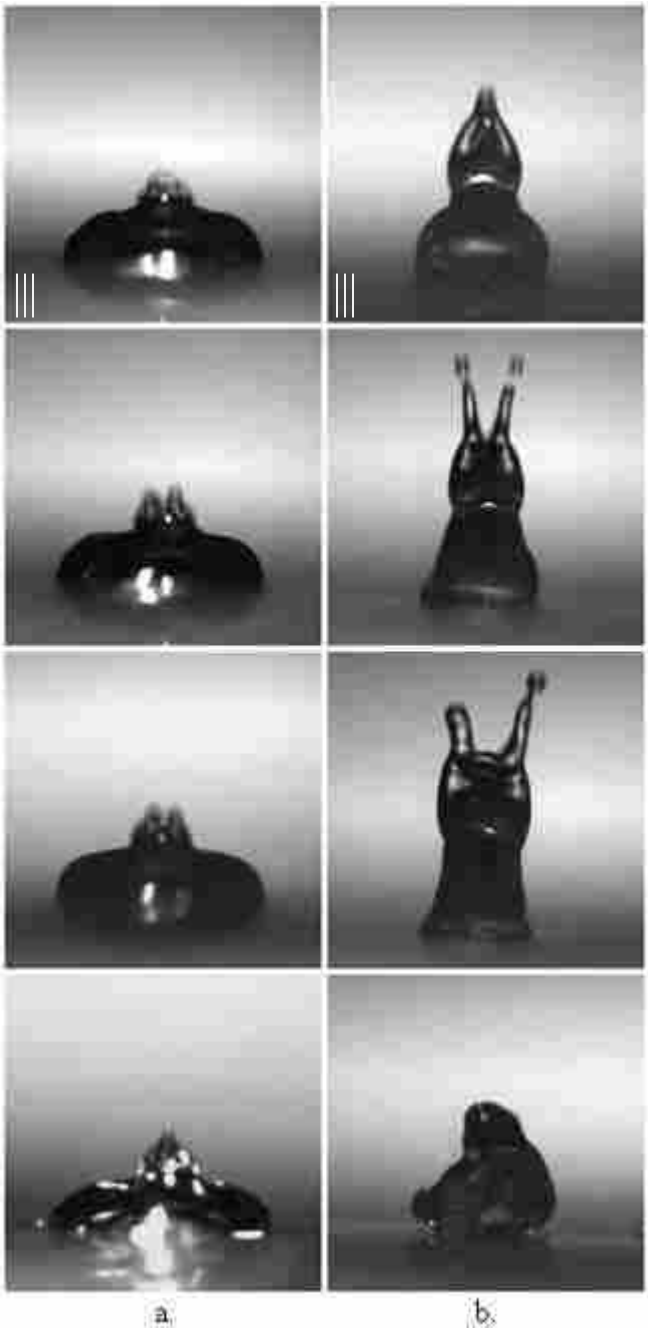

Figure 3-12: Images of the two-pronged jet phenomenon taken on a) a patterned uncoated surface (Case 3) and b) a patterned coated surface (Case 8). Values of *We* shown are, from top to bottom, a) 220, 250, 290, and 330; b) 195, 205, 250, and 270. All images were taken about 9 ms after impact. The top image of each set is at a value of *We* just before the onset of the two-pronged jets. The next two images of each set picture examples of two-pronged jets, and the final image of each set is at a value of *We* where the two-pronged jets are no longer observed.

ranges of *We*. All images shown in Fig. 3-12 were acquired at about 9 ms after impact. The top image of each set is at the *We* value just prior to the onset of the two-pronged jet phenomenon. The next two images of each set show examples of two-pronged jets for the two surfaces, and the final image of each set is at the *We* value where the two-pronged jets are no longer observed. In both cases, the two-pronged jet phenomena end when the instabilities associated with fingering affects the retraction process significantly. The third image of Fig. 3-8b already shows signs of losing stability, and the bottom image shows marked instability.

3.4.8 Ethanol on Patterned Coated Surfaces

The behavior when ethanol droplets impinge on the surfaces that are both coated and patterned is similar to the case when the surface is patterned but not coated. Again we see asymmetric spreading, with the fluid spreading further in the longitudinal direction, especially for $We < 100$. However, when the coating is added, the spreading due to wicking along the ribs is no longer observed. As a consequence of this, the droplet reaches a distinct maximum spread for the two spread directions at different times for $We < 100$. This is different from the uncoated case in that spreading does not continue in the longitudinal direction until the liquid evaporates. For $We > 100$, the maximum spread diameter is reached in both directions at a much more similar time. Figure 3-13 shows ethanol droplets impacting a patterned coated surface (Cases 7-8) for $We \approx 50$ from a) the transverse view, b) the longitudinal view, and c) the top view and $We \approx 250$ for d) the top view. For the lower *We* images (Fig. 3-13a-c) the frames show, from top to bottom, a droplet at impact (0 ms), at maximum spread in the transverse direction (3.7 ms), at maximum spread in the longitudinal direction (5.7 ms), as the transverse retraction reaches the center (9 ms), as the longitudinal retraction reaches the center (11.3 ms), and at equilibrium (22.1 ms). For the higher *We* set (Fig. 3-13d) the frames show, from top to bottom, a droplet at impact

(0 ms), at maximum spread in the transverse direction (2.3 ms), at maximum spread in the longitudinal direction (3.7 ms), as the fluid retracts in the fourth and fifth frames (11.7 ms and 17.3 ms), and at equilibrium (25.3 ms). For the low *We* case (Fig. 3-13a-c), $D_m/D_i \approx 2$ in the transverse direction, $D_m/D_i \approx 2.7$ in the longitudinal direction, and $u_j/u_i \approx 0.1$. For the high *We* case (Fig. 3-13d), $D_m/D_i \approx 3.1$ in the transverse direction, $D_m/D_i \approx 3.1$ in the longitudinal

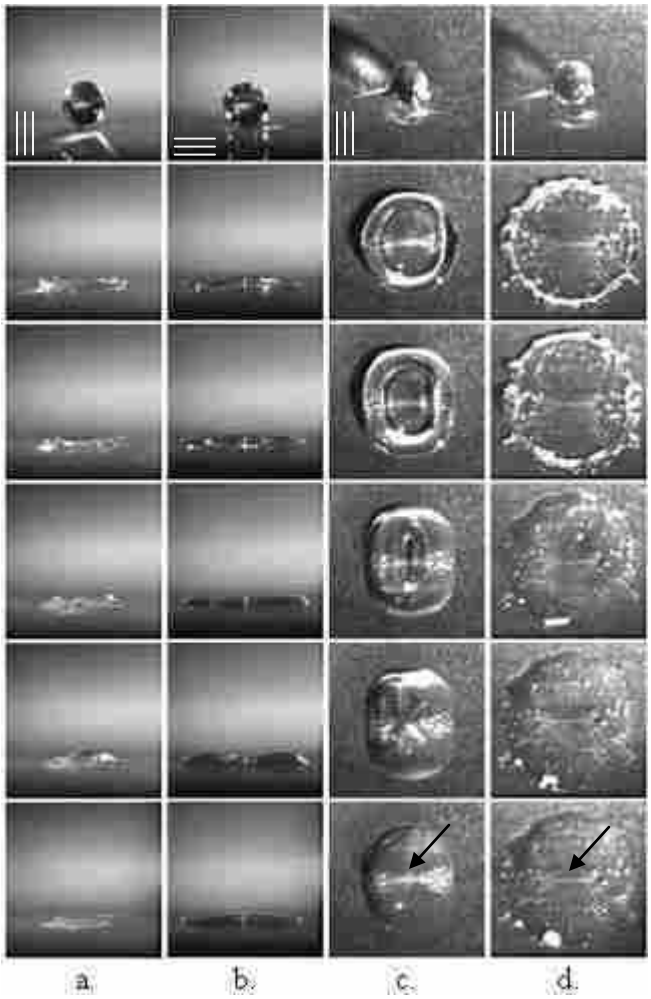

Figure 3-13: Images showing ethanol droplets impacting a patterned coated surface (Cases 7-8) for *We* ≈ 50 from a) the transverse view, b) the longitudinal view, and c) the top view and *We* ≈ 250 for d) the top view. The frames show, from top to bottom, a droplet at impact, at maximum spread in the transverse direction, at maximum spread in the longitudinal direction, as the transverse retraction reaches the center, as the longitudinal retraction reaches the center, and at equilibrium (a-c), and a droplet at impact, at maximum spread in the transverse direction, at maximum spread in the longitudinal direction, as the fluid retracts in the fourth and fifth frames, and at equilibrium (d).

direction, and $u_j/u_i < 0.1$. The side views (Figs. 3-13a-b), for the most part, do not illustrate the different events that can be observed from the top view images (Fig. 3-13c). When comparing the two top-view image sets in the figure, it can be seen that the high *We* experiments spread much less smoothly, but that both droplets remain pinned to the surface at all points where the fluid contacts it. Trapped air bubbles are evident in the cavities at certain points on the surface. The bottom frame of Figs. 3-13c and 3-13d most clearly illustrate the locations of bubbles by white regions on the surface, as indicated. The low *We* case shows a region of trapped bubbles that begins as a line at the impact location, and which propagates outwards in the transverse direction with the droplet spread. This same pattern is observed for the high *We* case, except the bubble region is much less coherent.

It has been noted that the liquid often spreads to a greater extent in the longitudinal direction than in the transverse direction, depending on conditions. Shown in Figs. 3-14 – 3-16 is the ratio of maximum spread in the longitudinal direction to the maximum spread in the transverse direction, D_{mL}/D_{mT}, for the micropatterned surfaces as a function of *We*. Figure 3-14 shows this ratio for the patterned uncoated surface (Cases 3-4). The ratio of maximum spread is the greatest for ethanol for $We < 100$, where D_{mL}/D_{mT} nearly reaches a value of 3. Water and the water/glycerine mixture both remain nearly at unity over the entire range of *We* tested for this surface type. The coated patterned surfaces are very similar to each other. In both there is an increase in the D_{mL}/D_{mT} ratio for $We > 100$ for water and the water/glycerine mixture. Also, the highest value for ethanol is near 2 instead of 3 as it is for the uncoated case.

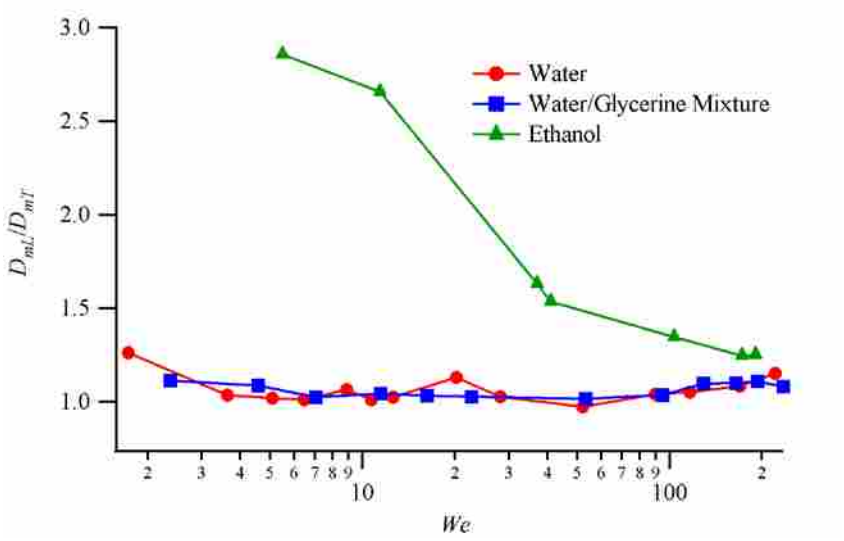

Figure 3-14: Ratio of maximum spread diameter in the longitudinal direction to the transverse direction, D_{mL}/D_{mT}, as a function of *We* for all three fluid types on the uncoated patterned surface (Cases 3-4).

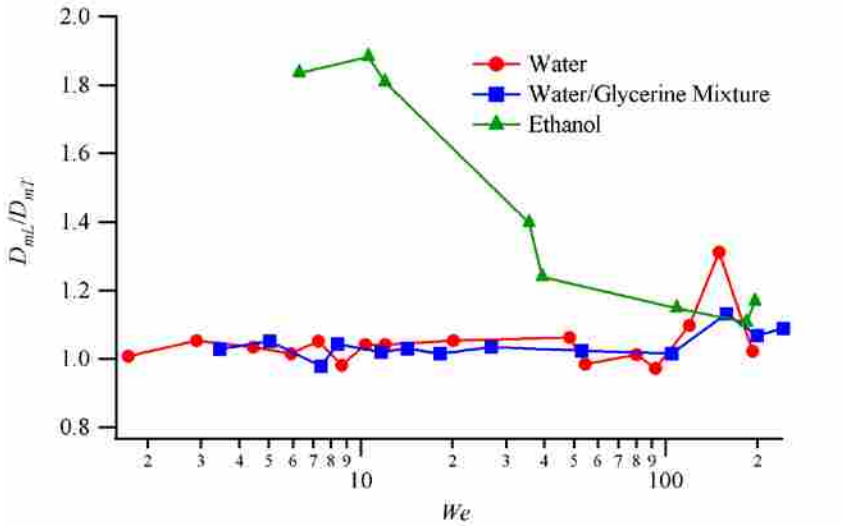

Figure 3-15: Ratio of maximum spread diameter in the longitudinal direction to the transverse direction, D_{mL}/D_{mT}, as a function of *We* for all three fluid types on the coated patterned surface with F_c = 0.8 (Cases 5-6).

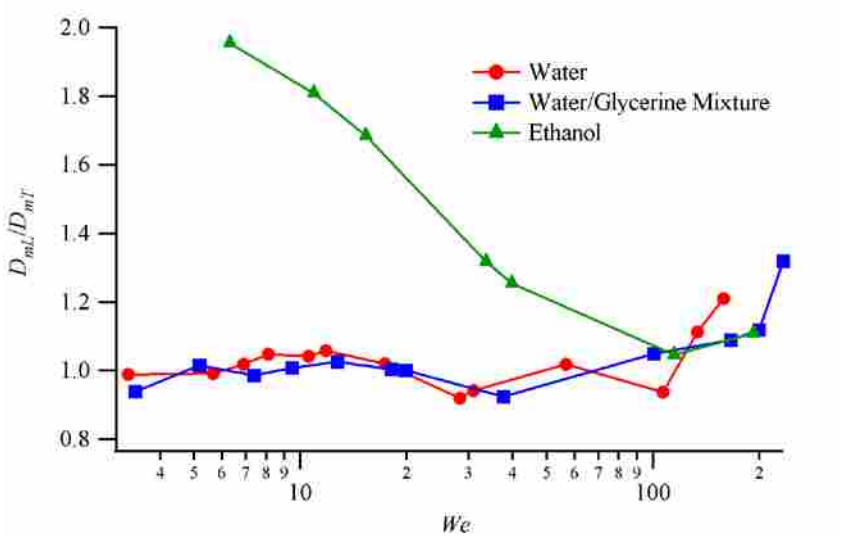

Figure 3-16: Ratio of maximum spread diameter in the longitudinal direction to the transverse direction, D_{mL}/D_{mT}, as a function of *We* for all three fluid types on the coated patterned surface with F_c = 0.93 (Cases 7-8).

3.4.9 Jet Formation

The experiments revealed a number of other interesting behaviors surrounding the ejected jets in addition to the splitting and oscillating jets. One phenomenon that was observed was the occurrence of a micro-jet. These jets, reported in previous literature (Bartolo et al., 2006) and in Chapter 2, have a significantly higher velocity and smaller radius than other jets. The micro-jet was only observed when water is the working fluid, and when *We* is small. Micro-jets are not observed for the smooth uncoated surface (Case 1). For the other surface types there is not a significant difference in the range of *We* where micro-jets occur, with the occurrence always in the range $5 < We < 15$. Occasionally the micro-jet is not observed in this range, as discussed in Chapter 2.

When the water/glycerine mixture is the fluid type, the ejected jets are smaller in diameter in some ranges of *We* than at others (about one tenth the diameter of the impacting droplet), although micro-jet behavior is never observed, and there are no large peaks in jet

ejection velocity. The range at which the smallest diameter jets can be observed varies significantly with surface type. Again, for the smooth uncoated surface (Case 1) significant jets are never observed. For the smooth coated surface (Case 2), the jets are very small in diameter from $We \approx 20$ up to the highest values of *We* tested. For the patterned surface with no coating (Cases 3-4), the jets are of smallest diameter in the range $10 < We < 30$. For the surfaces with both a coating and patterning (Cases 5-8) the jets are smallest in diameter in the range $7 < We < 25$. Figure 3-17 is a comparison of a) the micro-jet observed with pure water ($We = 7$) and b) a moderately small jet observed with the water/glycerine mixture ($We = 14$). The images show, from top to bottom, the droplet at impact, at maximum spread diameter, as the jet is being ejected, and as the jet continues to rise for the bottom two frames. Both image sets were taken on a superhydrophobic surface (Cases 7-8). It is interesting to note that for the case of pure water, where the micro-jet behavior is observed, that the droplet hasn't fully collapsed onto the surface at the time when the maximum diameter has been reached. This is indicated in the second frame of Fig. 3-17a. Another interesting point, indicated in the bottom frame of Fig. 3-17a, is that when micro-jet behavior is observed, an air bubble is trapped in the droplet. This air bubble entrapment was observed to happen almost universally when the micro-jet behavior prevailed, and has been observed previously in conjunction with micro-jets (Bartolo et al., 2006). Ethanol never issues comparable jets since it exhibits hydrophilic behavior on all surfaces tested.

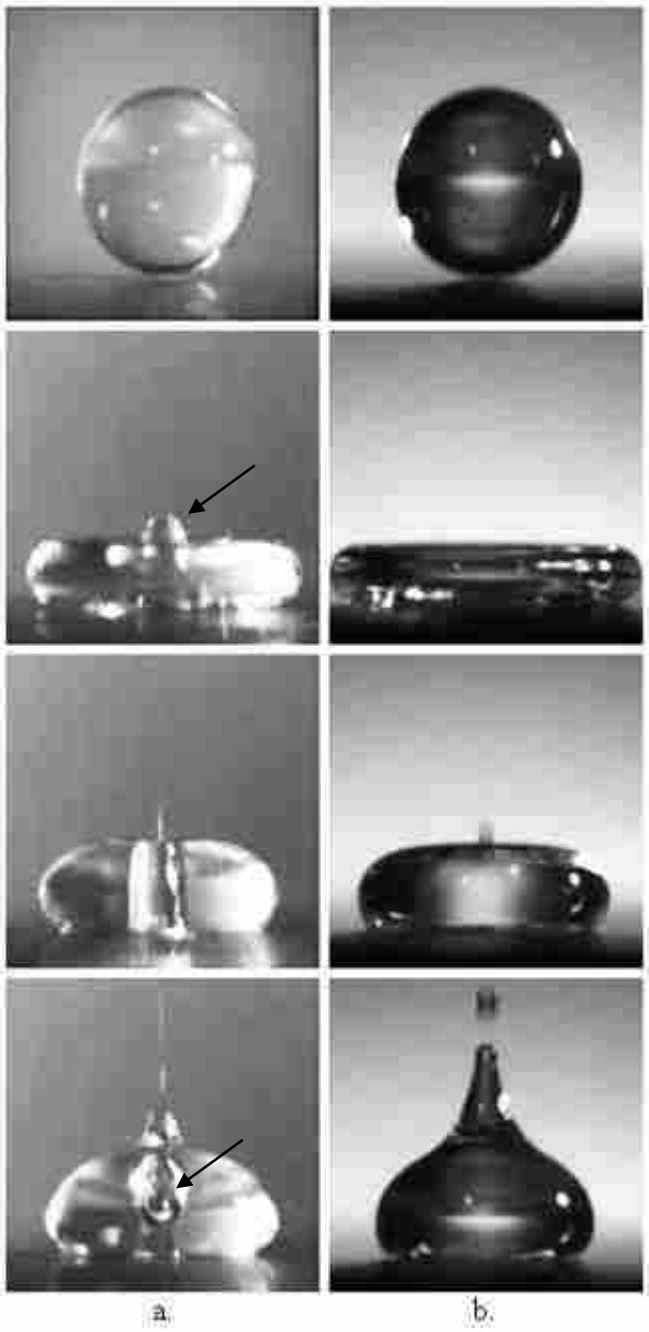

Figure 3-17: Images of a) a water droplet impact test where a micro-jet is observed (*We* = 7) and b) a water/glycerine mixture droplet impact test were a moderately small jet is observed (*We* = 14). Both image sets were taken on a superhydrophobic surface (Case 7).

3.4.10 Droplet Clustering and Formation

Another phenomenon observed in droplet tests on surfaces patterned with ribs and cavities was the occurrence of a repeatable pattern seen during the spreading and retracting process of four clusters of fluid. Shown in Fig. 3-18 are representative images of this phenomenon for a) water, b) the water/glycerine mixture, and c) ethanol. For water, the four clusters are more difficult to see due to the fingering that also occurs. However, there are still four distinct clusters present, and they are indicated on the figure. Measurements have shown that these fluid clusters are always located at about 29.4° from the transverse direction. This pattern can be observed for $We > 150$ for all fluid and surface types (patterned surfaces). The pattern is less distinct on surfaces that do not have a hydrophobic coating, but is consistently present in the range of *We* noted. At higher *We*, when the droplet splashes peripherally, the pattern becomes more difficult to see but can still be observed. For the water/glycerine mixture, it was seen that often the first satellite droplets released peripherally began at these four points. Because this is observed for all fluid types, and whether or not there a coating is present, it can be concluded that this phenomenon is an effect of the rib and cavity features on the surface. More information is needed to better understand the exact cause of the four clusters of liquid phenomenon and the angle of 29.4°.

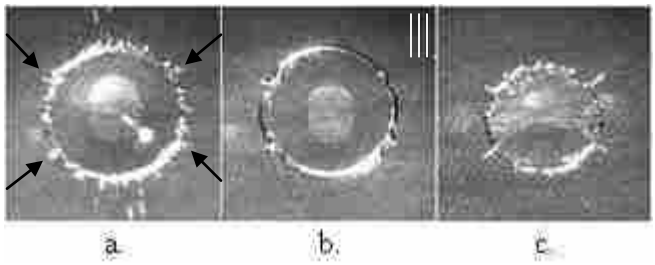

Figure 3-18: Images depicting the occurrence of four clusters of fluid for a) water, b) the water/glycerine mixture, and c) ethanol on a patterned coated surface (Cases 7-8). For the experiments shown $We \approx 250$. The images shown were taken just before maximum spread was reached.

It was further observed that when droplets impacted surfaces with rib and cavity micro-structuring at high values of *We* such that satellite droplets were released peripherally, the peripheral droplets favored the longitudinal direction. At the earliest onset of the peripheral splash, droplets are observed to only travel in the longitudinal direction. As *We* increases, the released droplets begin spreading, increasingly towards the transverse direction. An example of this can be seen in Fig. 3-19, where a water droplet is pictured impinging upon a surface patterned with ribs and cavities (Cases 7-8). For this case, $We \approx 300$. Frames show a) the droplet at impact, b) as the first released droplets can be seen (indicated on figure), and c) as the droplet continues to spread, but before maximum spread has been reached.

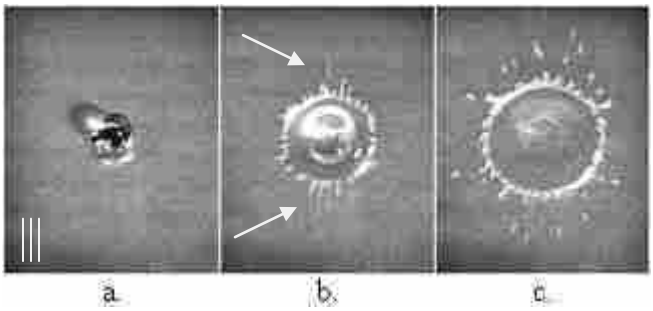

Figure 3-19: Images of a water droplet impinging upon a coated surface patterned with ribs and cavities (Cases 7-8). For the case pictured, *We* ≈ 300. Frames show the droplet a) at impact, b) as the first released droplets can be seen, and c) as the droplet continues to spread.

3.4.11 Flow Visualization

A small number of experiments were performed using milk droplets instead of the other fluid types. Further, the milk was seeded with fine graphite powder. The purpose of these tests was to visualize the fluid motion of the droplet. The surface tension is somewhat less, and the viscosity is somewhat more than for pure water, with the surface tension σ = 47.3 mN/m, and viscosity μ = 1.53 mPa·s (Kristensen et al., 1997). Shown in Fig. 3-20 is a comparison of a milk

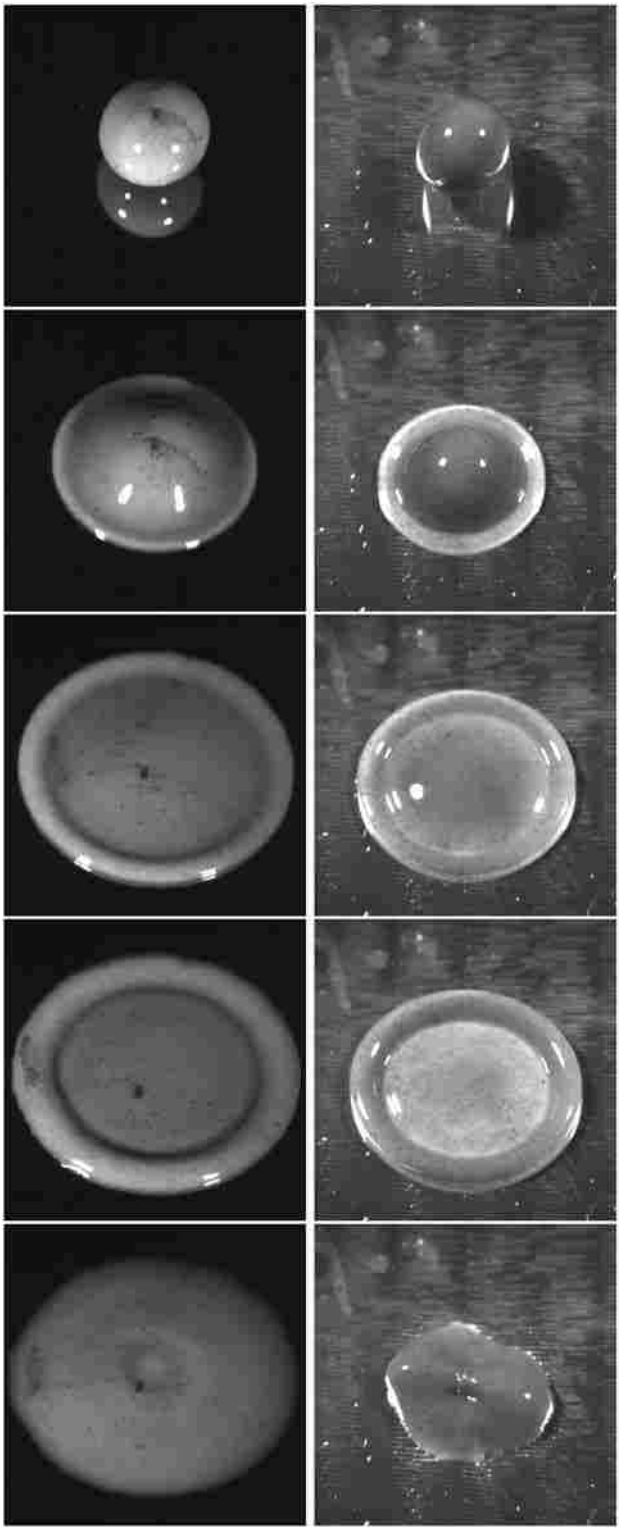

a. b.

Figure 3-20: Images of milk droplets impacting a) a smooth uncoated surface, and b) a coated patterned surface. Frames show, from top to bottom, a droplet at impact, two frames as it is spreading outward, at maximum spread, and as a jet is ejected.

droplet impacting a) a smooth uncoated surface (Case 1) and b) a coated patterned surface (Cases 7-8). Frames show, from top to bottom, the droplet at impact, as it is spreading, at maximum diameter, and as a jet is being ejected. From the images, it can be learned that the fluid moves somewhat differently between the two cases. For the hydrophilic case (Fig. 3-20a), the fluid can be seen moving outward from the center and over the top of the rim as the droplet spreads on the surface. For the superhydrophobic case (Fib. 3-20b), the fluid can be seen moving outward in the flat area in the center, but not over the top of the rim. Rather, the fluid on the rim remains stationary with respect to the rim. The fluid, therefore, is moving along the surface and in to the rim from beneath. A schematic for these two scenarios can be seen in Fig. 3-21 for a) the hydrophilic case and b) the superhydrophobic case. It is assumed that the flow patterns shown here hold for water and other fluids when hydrophilic and superhydrophobic behavior prevails. Experiments dealing with contact angles between these two extremes most likely display intermediate behavior.

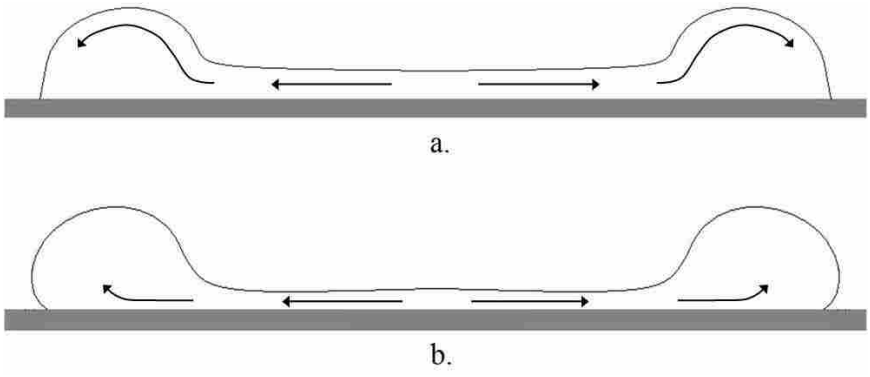

Figure 3-21: Schematic representation of fluid motion during spreading for a milk droplet on a) a smooth uncoated surface (Case 1) and b) a coated patterned surface (Cases 7-8).

3.5 Conclusions

Qualitative results from droplet impact tests have been presented. The experiments demonstrated that instabilities resulting in fingering are dependent upon surface and fluid type, although not dependent upon the static contact angle. The onset of fingering occurred at a lower *We* for water than for the other liquid types. The onset of peripheral splashing was observed be dependent upon static contact angle, and it generally occurred at a lower *We* for a higher static contact angle. The viscous water/glycerine mixture was an exception to this trend, as an increase in contact angle resulted in a higher *We* at the onset of peripheral splashing.

For surfaces with the rib and cavity micro-roughness, the droplet spreading and retraction are asymmetric. For uncoated patterned surfaces, liquid was observed to penetrate the cavities at a larger area beneath the impact location than for the coated patterned (superhydrophobic) surfaces when water or the water/glycerine mixture was the working fluid. The liquid remained pinned to the surface at these locations for the uncoated case, but was pulled out of the cavities for the coated case. For ethanol, the liquid penetrated the cavities at all points of contact and remained pinned. Spreading continued along the ribs due to capillary forces until evaporation for the uncoated case.

Other interesting jet behavior was also observed. The occurrence of two-pronged and oscillating jets for water/glycerine tests occurred during droplet retraction for surfaces with rib and cavity features. The oscillating and splitting jets were observed to be much stronger on the superhydrophobic surfaces than on the surfaces with patterning but no hydrophobic coating. Micro-jets with very high velocities were observed for water, and smaller diameter jets were observed with the water/glycerine mixture in certain ranges of *We,* depending on the surface type. An interesting spread pattern of four liquid droplets clustered at about 30° from the

transverse direction was observed for $We > 150$ for all three liquid types. Finally, experiments designed to visualize the flow revealed a difference between fluid motion in the rim for the hydrophilic and superhydrophobic cases.

4 CONCLUSIONS

This thesis has presented experimental results for droplet impingement experiments performed on superhydrophobic surfaces. The fluid types used in these tests were pure water, a 50/50 water/glycerine mixture, and ethanol. Data from the following surface types were also included for comparison: smooth uncoated, smooth coated, and structured uncoated. Data were acquired with the camera view in both the longitudinal direction (when the fluid motion was parallel to the ribs) and the transverse direction (when the fluid motion is perpendicular to the ribs). Image analysis software was used to calculate the following parameters for each experiment: Weber number, Ohnesorge number, maximum spread diameter, D_m, time between droplet impact and maximum spread diameter, t_D, time between droplet impact and vertical jet ejection, t_j, and jet velocity, u_j. The data acquired covered Weber numbers ranging from 1 to 500, and Ohnesorge numbers ranging from 0.002 to 0.015. The superhydrophobic surfaces exhibited cavity fractions of 0.8 and 0.93. The data reveal only modest differences between superhydrophobic surfaces and other surfaces when considering the maximum spread diameter, although the time between impact and maximum spread diameter and the time between impact and jet ejection are modestly less for superhydrophobic surfaces than for other hydrophobic surfaces. The differences are most pronounced at higher *We* and for fluids of greater viscosity. The trends are slightly different when in the hydrophobic regime as opposed to the hydrophilic regime. Measurements of the issuing jet that forms during droplet rebound showed that in general higher jet velocities prevail for the superhydrophobic surfaces than for the other surfaces

considered. A micro-jet regime was observed where water droplets were observed to have very high jet velocities, nearly 20 times the impact velocity. The data were compared to an empirical model developed by Mao et al. (1997). This model predicts maximum spread diameter, and fit reasonably well when $We > 70$, but over-predicts maximum spread diameter for low *We*. A recent analytical model derived by Attane et al. (2007) was also compared to the experimental results and demonstrated good agreement with data taken on grooved superhydrophobic surfaces in many cases. However, the model does not account for surface anisotropy or apparent slip at the solid-liquid interface and these are two points that should be considered in model refinement.

Qualitative results from droplet impact tests have also been presented. The experiments demonstrated that instabilities resulting in fingering are dependent upon surface and fluid type, although not dependent upon the static contact angle. The onset of fingering occurred at a lower *We* for water than for the other liquid types. The onset of peripheral splashing was observed be dependent upon static contact angle, and it generally occurred at a lower *We* for a higher static contact angle. The viscous water/glycerine mixture was an exception to this trend, as an increase in contact angle resulted in a higher *We* at the onset of peripheral splashing.

For surfaces with the rib and cavity micro-roughness, the droplet spreading and retraction processes are asymmetric. For uncoated patterned surfaces, liquid was observed to penetrate the cavities at a larger area beneath the impact location than for the coated patterned (superhydrophobic) surfaces when water or the water/glycerine mixture was the working fluid. The liquid remained pinned to the surface at these locations for the uncoated case, but was pulled out of the cavities for the coated case. For ethanol, the liquid penetrated the cavities at all points of contact and remained pinned. Spreading continued along the ribs due to capillary forces until evaporation for the uncoated case.

Other interesting jet behavior was also observed that have not previously been observed. The occurrence of two-pronged and oscillating jets for water/glycerine tests occurred during droplet retraction for surfaces with rib and cavity features. The oscillating and splitting jets were observed to be much stronger on the superhydrophobic surfaces than on the surfaces with patterning but no hydrophobic coating. In addition to the micro-jets for water, smaller diameter jets were observed with the water/glycerine mixture in *We* ranges that are surface type dependent. An interesting spread pattern of four liquid droplets clustered at about 30° from the transverse direction was observed for $We > 150$ for all three liquid types. Finally, experiments designed to visualize the fluid motion revealed a difference between behavior on hydrophilic and superhydrophobic surfaces.

There are some areas where further work is needed. Very little was learned about the effect of varying the cavity fraction. It is recommended that a variety of cavity fractions be tested, varying perhaps from $F_c = 0.25$ to $F_c = 0.99$. This would give more information about the effect of the cavity fraction, and what cavity fraction is needed to obtain certain results. Also, it would be helpful to investigate higher values of the Ohnesorge number, which could be done most easily by further increasing the viscosity of the test fluid. There is also room to obtain more information about hydrophilic behavior on anisotropic surfaces, such as the ethanol tests on the patterned surfaces with or without a hydrophobic coating. Finally, incorporating apparent slip and surface anisotropy in an analytical model predicting droplet behavior upon impact could be investigated.

REFERENCES

Attane, P., Girard, F., Morin, V. (2007), "An energy balance approach of the dynamics of drop impact on a solid surface," *Phys. Fluids*, **19**, 012101.

Bartolo, D., Bouamrirene, F., Verneuil, É., Buguin, A., Silberzan, P., Moulinet, S. (2006a), "Bouncing or sticky droplets: Impalement transitions on superhydrophobic micropatterned surfaces," *Europhys. Lett.*, **74**, 299.

Bartolo, D., Josserand, C., Bonn, D. (2006b), "Singular jets and bubbles in drop impact," *Phys. Rev. Lett.*, **96**, 124501.

Brunet, P., Lapierre, F., Thomy, V., Coffinier, Y., Boukherroub, R. (2008), "Extreme resistance of superhydrophobic surfaces to impalement: Reversible electrowetting related to the impacting/bouncing drop test," *Langmuir*, **24**, 11203.

Bussmann, M., Chandra, S., Mostaghimi, J. (2000), "Modeling the splash of a droplet impacting a solid surface," *Phys. Fluids*, **12** (12), 3121.

Byun, D., Kim, J., Ko, H. S., Park, H. C. (2008), "Direct measurement of slip flows in superhydrophobic microchannels with transverse grooves," *Phys. Fluids*, **20**, 113601.

Clanet, C., Beguin, C., Richard, D., Quéré, D. (2004), "Maximal deformation of an impacting drop," *J. Fluid Mech.*, **517**, 199.

Davies, J., Maynes, D., Webb, B. W., Woolford, B. (2006), "Laminar flow in a microchannel with super-hydrophobic walls exhibiting transverse ribs," *Phys. Fluids*, **18**, 087110.

Deng, T., Varanasi, K. K., Hsu, M., Bhate, N., Keimel, C., Stein, J., Blohm, M. (2009), "Nonwetting of impinging droplets on textured surfaces," *Appl. Phys. Lett.*, **94**, 133109.

Deng, Q., Anilkumar, A. V., Wang, T. G. (2007), "The role of viscosity and surface tension in bubble entrapment during drop impact onto a deep liquid pool," *J. Fluid Mech.*, **578**, 119.

Fukagata, K., Kasagi, N. (2006), "A theoretical prediction of frictional drag reduction in turbulent flow by superhydrophobic surfaces," *Phys. Fluids*, **18**, 051703.

German, G., Bertola, V. (2009), "Review of drop impact models and validation with high-viscosity newtonian fluids," *At. Sprays*, **19**, 787.

Hyväluoma, J., Timonen, J. (2009), "Impact states and energy dissipation in bouncing and non-bouncing droplets," *J. Stat. Mech.*, P06010.

Incropera, F. P., Dewitt, D. P., Bergman, T. L., Lavine, A. S. (2006), *Fundamentals of Heat and Mass Transfer 6E*, John Wiley & Sons, Inc., 949.

Jeffs, K., Maynes, D., Webb, B. W. (2010), "Prediction of turbulent channel flow with superhydrophobic walls consisting of micro-ribs and cavities oriented parallel to the flow direction," *Int. J. Heat Mass Transfer*, **53**, 786.

Jung, Y. C., Bhushan, B. (2007), "Wetting transition of water droplets on superhydrophobic patterned surfaces," *Scripta Materialia*, **57**, 1057.

Jung, Y. C., Bhushan, B. (2008), "Dynamic effects of bouncing water droplets on superhydrophobic surfaces," *Langmuir*, **24**, 6262.

Jung, Y. C., Bhushan, B. (2009), "Dynamic effects induced transition of droplets on biomimetic superhydrophobic surfaces," *AIChE*, **55** (8), 1983.

Kannan, R., Sivakumar, D. (2008a), "Drop impact process on a hydrophobic grooved surface," *Colloids Surf. A*, **317**, 694.

Kannan, R., Sivakumar, D. (2008b), "Impact of liquid drops on a rough surface comprising microgrooves," *Exp. Fluids*, **44**, 927.

Kim, H. Y., Chun, J. H. (2001), "The recoiling of liquid droplets upon collision with solid surfaces," *Phys. Fluids*, **13**, 643.

Kristensen, D., Jensen, P. Y., Madsen, F., Birdi, K. S. (1997), "Rheology and surface tension of selected processed dairy fluids: influence of temperature," *J. Dairy Sci.*, **80**, 2282.

Lau, K. K. S., Bico, J., Teo, K. B. K., Chhowalla, M., Amaratunga, G. A. J., Milne, W. I., McKinley, G.. H., Gleason, K. K. (2003), "Superhydrophobic carbon nanotube forests," *Nano Lett.*, **3**, 1701.

Lauga, E., Stone, H. (2003), "Effective slip in pressure-driven Stokes flow," *J. Fluid Mech.*, **489**, 55.

Lee, C., Choi, C. H., Kim, C. J. (2008), "Structured surfaces for giant liquid slip," *Phys. Rev. Lett.*, **101**, 064501.

Li, X., Ma, X., Lan, Z. (2009a), "Behavioral patterns of drop impingement onto rigid substrates with a wide range of wettability and different surface temperatures," *AIChE*, **55** (8), 1983.

Li, X., Ma, X., Lan, Z. (2009b), "Dynamic behavior of the water droplet impact on a textured hydrophobic/superhydrophobic surface: the effect of the remaining liquid film arising on the pillars' tops on the contact line," *Langmuir*, **26** (7), 4831.

Mao, T., Kuhn, D. C. S., Tran, H. (1997), "Spread and rebound of liquid droplets upon impact of flat surfaces," *AIChE*, **43**, 2169.

Martell, M. B., Perot, J. B., Rothstein, J. P. (2009), "Direct numerical simulations of turbulent flows over superhydrophobic surfaces," *J. Fluid Mech.*, **620**, 3.

Maynes, D., Jeffs, K., Woolford, B., Webb, B. W. (2007), "Laminar flow in a microchannel with hydrophobic surface patterned microribs oriented parallel to the flow direction," *Phys. Fluids*, **19**, 093603.

Min, T., Kim, J. (2004), "Effects of hydrophobic surface on skin-friction drag," *Phys. Fluids*, **16**, L55.

Munson, B. R., Young, D. F., Okiishi, T. H. (2006), *Fundamentals of Fluid Mechanics 5E*, John Wiley & Sons, Inc.

Okumura, K., Chevy, F., Richard, D., Quéré, D., Clanet, C. (2003), "Water spring: A model for bouncing drops," *Europhys. Lett.*, **62**, 237.

Ou, J., Perot, B., Rothstein, J. P. (2004), "Laminar drag reduction in microchannels using ultrahydrophobic surfaces," *Phys. Fluids*, **16**, 4635.

Ou, J., Rothstein, J. P. (2005), "Direct velocity measurements of the flow past drag-reducing ultrahydrophobic surfaces," *Phys. Fluids*, **17**, 103606.

Pasandideh-Fard, M., Qiao, Y. M., Chandra, S., Mostaghimi, J. (1996), "Capillary effects during droplet impact on a solid surface," *Phys. Fluids*, **8** (3), 650.

Renardy, Y., Popinet, S., Duchemin, L., Renardy, M., Zaleski, S., Josserand, C., Drumright-Clarke, M. A., Richard, D., Clanet, C., Quéré, D. (2003), "Pyramidal and toroidal water drops after impact on a solid surface," *J. Fluid Mech.*, **484**, 69.

Reyssat, M., Pépin, A., Marty, F., , Y. Chen, Quéré, D. (2006), "Bouncing transitions on mictrotextured materials," *Europhys. Lett.*, **74**, 306.

Richard, D., Clanet, C., Quéré, D. (2002), "Surface phenomena: Contact time of a bouncing drop," *Nature*, **417**, 811.

Rioboo, R., Tropea, C., Marengo, M. (2001), "Outcomes from a drop impact on solid surfaces," *At. Sprays*, **11**, 155.

Rioboo, R., Voué, M., Vaillant, A., De Coninck, J. (2008), "Drop impact on porous superhydrophobic polymer surfaces," *Langmuir*, **24** (24), 14074.

Rothstein, J. P. (2010), "Slip on superhydrophobic surfaces," *Annu. Rev. Fluid Mech.*, **42**, 89.

Tuteja, A., Choi, W., Mabry, J. M., McKinley, G. H., Cohen, R. E. (2008), "Robust omniphobic surfaces," *AIChE*, **55** (8), 1983.

Wang, Z., Lopez, C., Hirsa, A., Koratkar, N. (2007), "Impact dynamics and rebound of water droplets on superhydrophobic carbon nanotube arrays," *Appl. Phys. Lett.*, **91**, 023105.

Weisberg, S. (2005), *Applied Linear Regression 3E*, John Wiley & Sons, Inc., 19.

Woolford, B. (2009), "Laminar and turbulent flow of a liquid through channels with superhydrophobic walls exhibiting alternating ribs and cavities," Dissertation, Brigham Young University.

Woolford, B., Maynes, D., Webb, B. W. (2009a), "Liquid flow through microchannels with grooved walls under wetting and superhydrophobic conditions," *Microfluid. Nanofluid.*, **7**, 121.

Woolford, B., Prince, J., Maynes, D., Webb, B. W. (2009b), "Particle image velocimetry characterization of turbulent channel flow with rib patterned superhydrophobic walls," *Phys. Fluids*, **21**, 085106.

Yarin, A. L. (2006), "Drop impact dynamics: Splashing, spreading, receding, bouncing…" *Annu. Rev. Fluid Mech.*, **38**, 159.

Yeomans, J. M., Kusumaatmaja, H. (2007), "Modelling drop dynamics on patterned surfaces," *Bull. Pol. Ac.: Tech.*, **55**, 203.

APPENDIX A. ADDITIONAL DATA

The data presented in Chapter 2 is only a portion of the total data collected through the experiments. The remainder of the data collected will be given here, organized according to surface type. Some figures will repeat data already shown in the interest of uniformity.

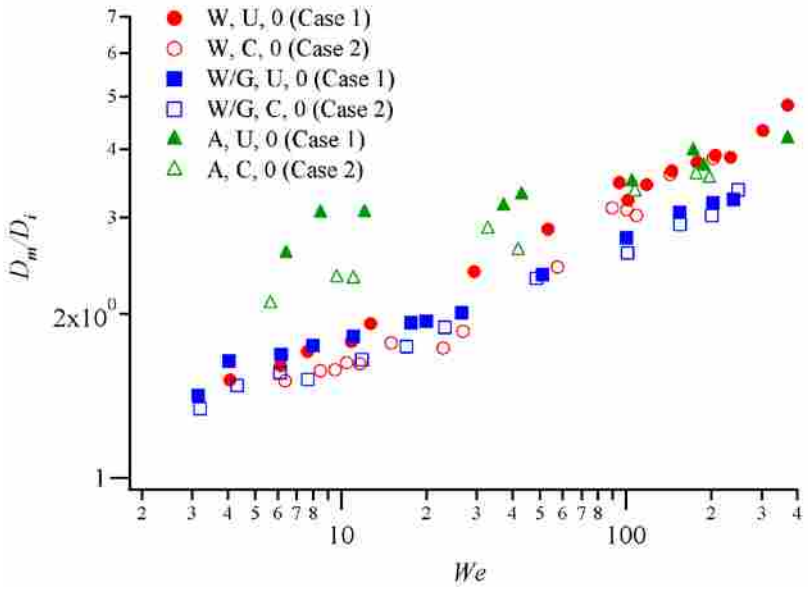

Figure A-1: Normalized maximum spread diameter, D_m/D_i, as a function of *We* for droplets of three fluid types impinging on a smooth surface, with and without a coating (Cases 1-2). Legend code is fluid type (W – water, W/G – water/glycerine mixture, A – ethyl alcohol), coated or uncoated (C – coated, U – uncoated), cavity fraction (0 – no grooves, F_c = 0.8 or 0.93), and spread direction (L – longitudinal, T – transverse).

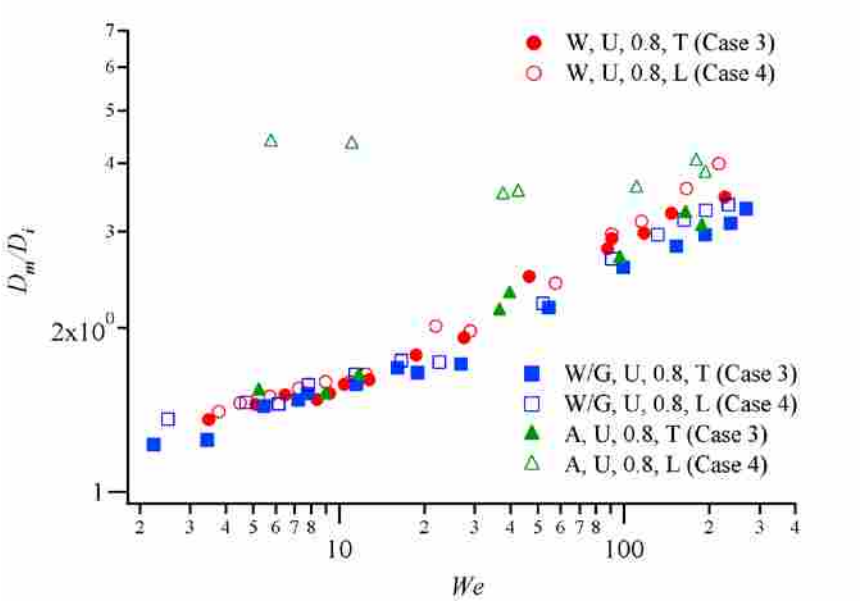

Figure A-2: Normalized maximum spread diameter, D_m/D_i, as a function of *We* for droplets of three fluid types impinging on the patterned uncoated surface (Cases 3-4). See Fig. A-1 caption for legend key.

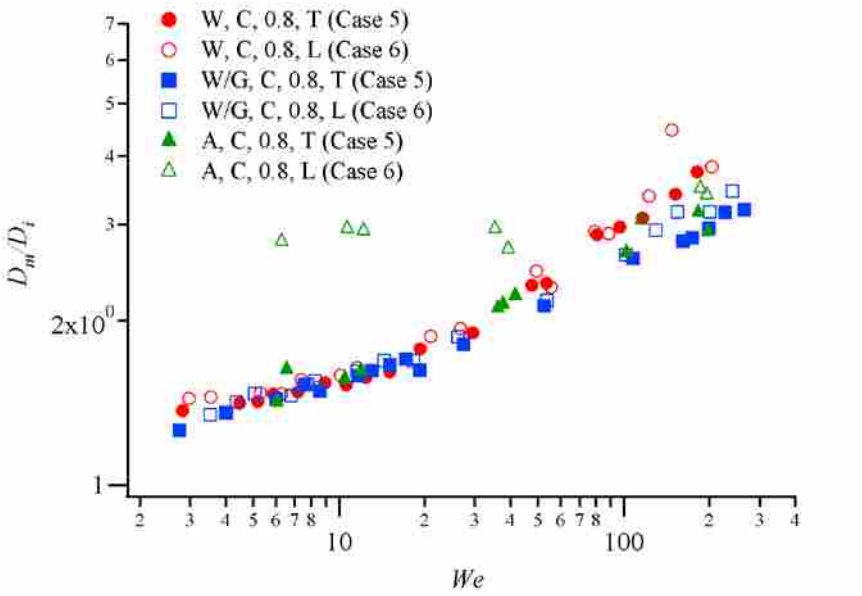

Figure A-3: Normalized maximum spread diameter, D_m/D_i, as a function of *We* for droplets for three fluid types impinging on a superhydrophobic surface with F_c = 0.8 (Cases 5-6). See Fig. A-1 caption for legend key.

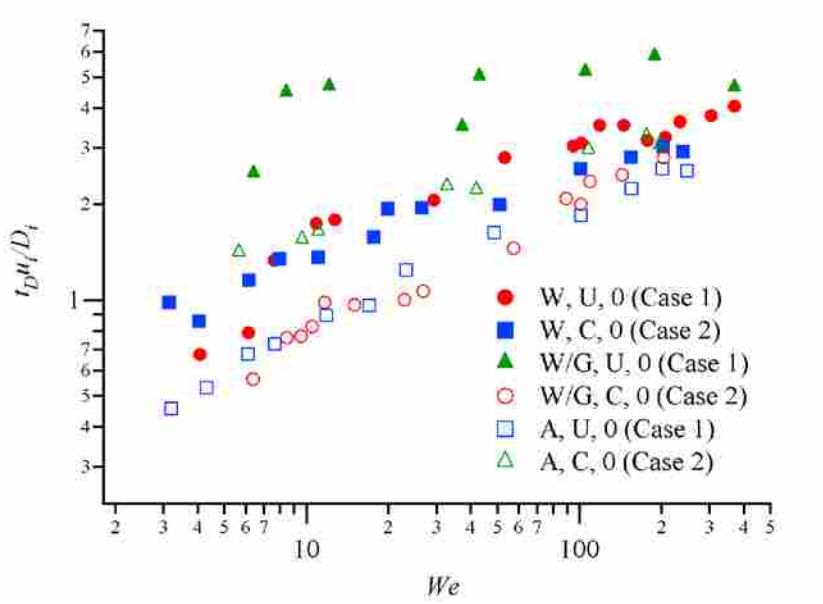

Figure A-4: Normalized time delay between droplet impact and the point when the maximum spread diameter is attained, $t_D u_i/D_i$, as a function of *We* for all three fluid droplet types on smooth surfaces with or without a hydrophobic coating (Cases 1-2). See Fig. A-1 caption for legend key.

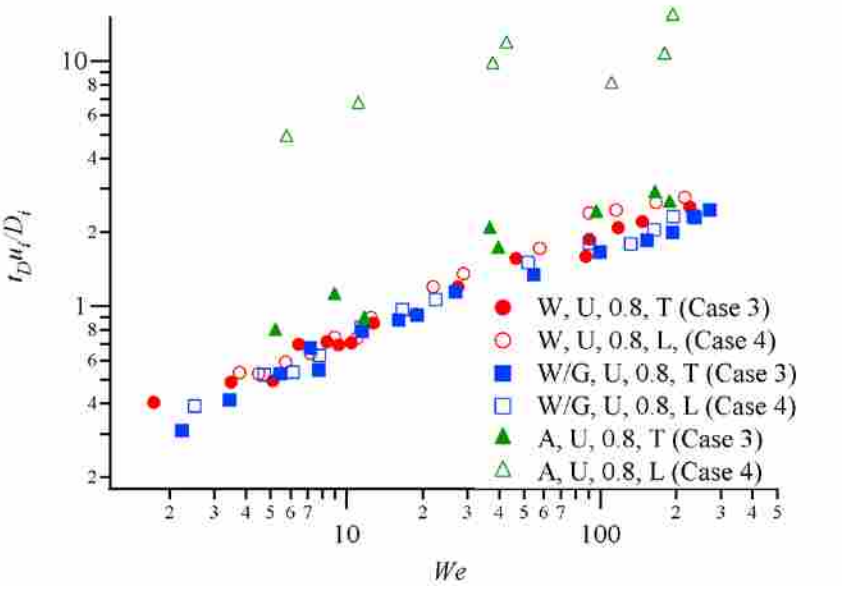

Figure A-5: Normalized time delay between droplet impact and the point when the maximum spread diameter is attained, $t_D u_i/D_i$, as a function of *We* for all three fluid droplet types on an uncoated micropatterned surface with F_c = 0.8 (Cases 3-4). See Fig. A-1 caption for legend key.

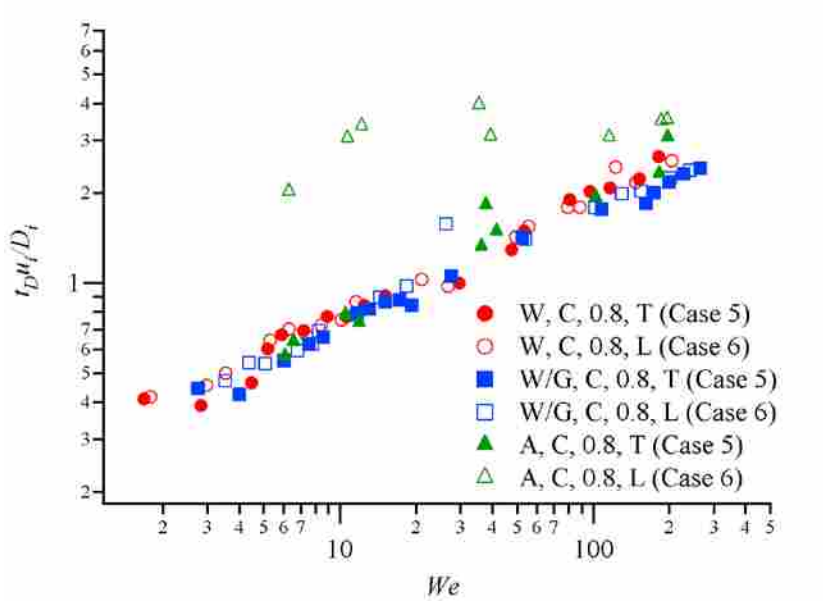

Figure A-6: Normalized time delay between droplet impact and the point when the maximum spread diameter is attained, $t_D u_i/D_i$, as a function of *We* for all three fluid droplet types on a superhydrophobic surface with F_c = 0.8 (Cases 5-6). See Fig. A-1 caption for legend key.

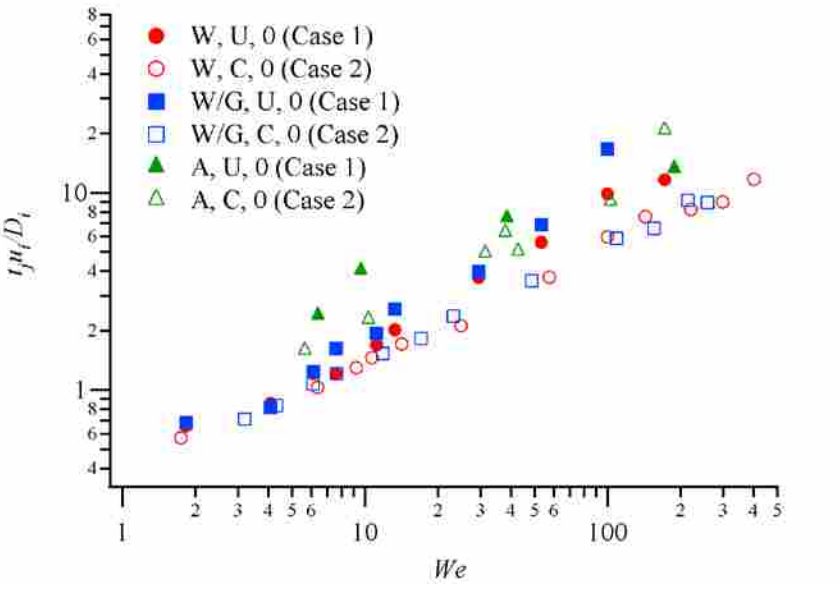

Figure A-7: Normalized time delay between droplet impact and the point when the liquid jet forms, $t_j u_i/D_i$, as a function of *We* for all three liquid droplet types impinging on smooth surfaces with or without a hydrophobic coating (Cases 1-2). See Fig. A-1 caption for legend key.

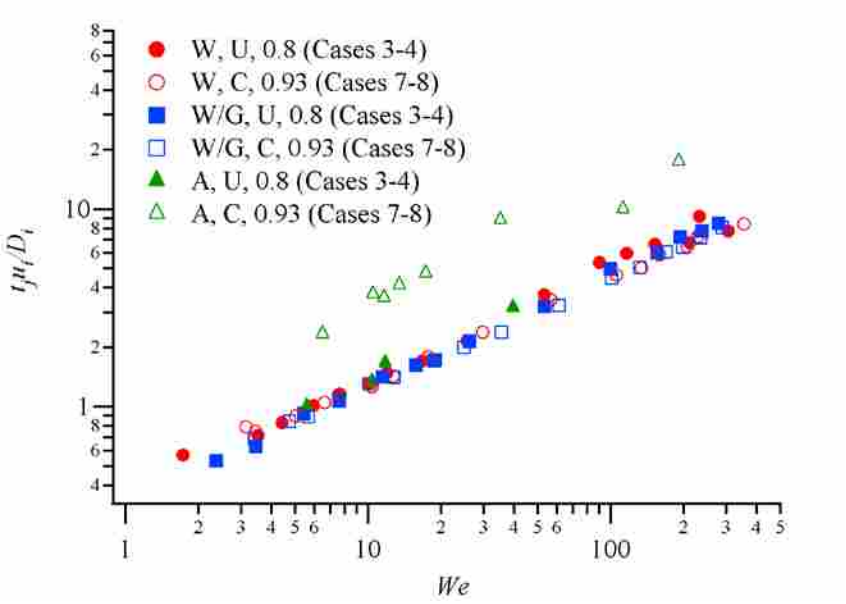

Figure A-8: Normalized time delay between droplet impact and the point when the liquid jet forms, $t_j u_i/D_i$, as a function of *We* for all three liquid droplet types impinging on micropatterned surfaces, with and without a hydrophobic coating (Cases 3-4 and 7-8). See Fig. A-1 caption for legend key.

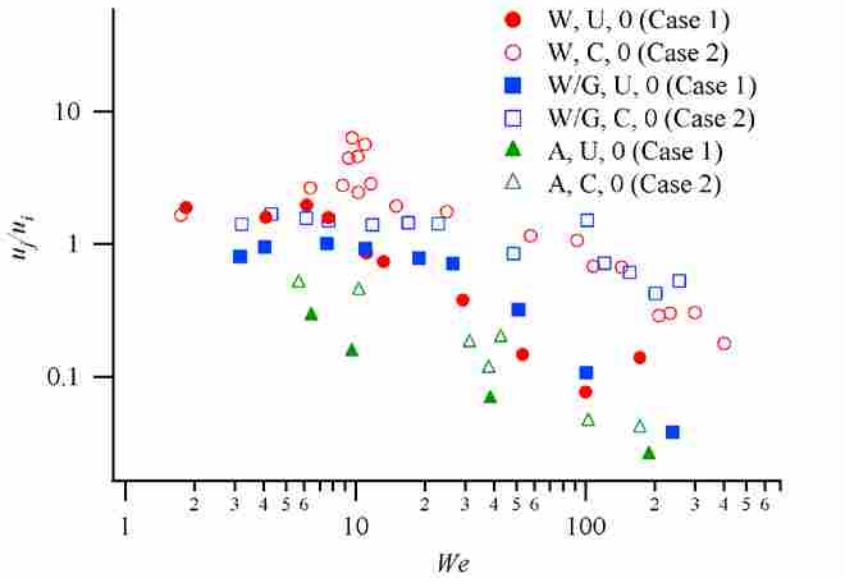

Figure A-9: Normalized jet velocity, u_j/u_i, as a function of *We* on smooth surfaces, with and without a hydrophobic coating (Cases 1-2). See Fig. A-1 caption for legend key.

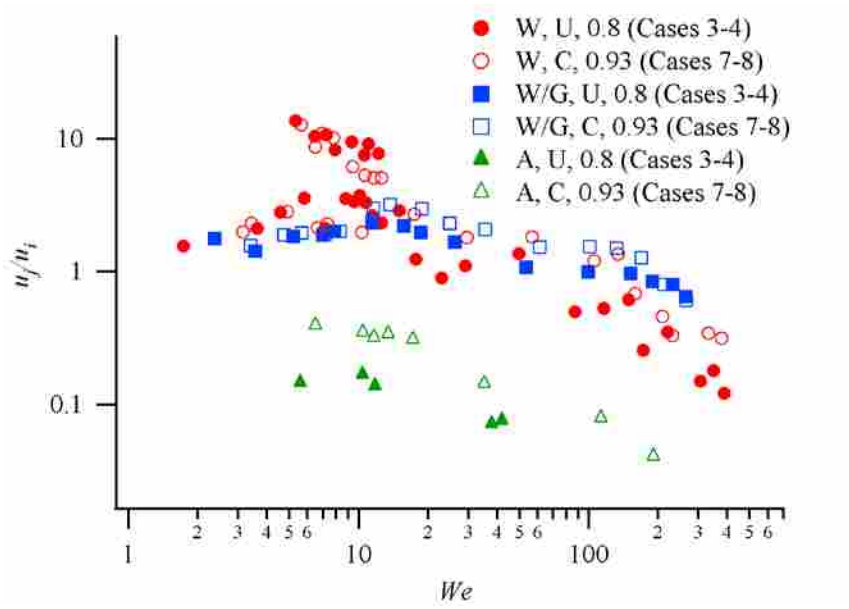

Figure A-10: Normalized jet velocity, u_j/u_i, as a function of *We* on micropatterned surfaces, with and without a hydrophobic coating (Cases 3-4 and 7-8). See Fig. A-1 caption for legend key.

APPENDIX B. MATLAB CODES

B.1 Description

These codes are associated with Chapter 2. The codes used to analyze image sets will be given, and then the codes used to plot the analytical models will be given.

B.2 Codes for Image Analysis

```
% This program reads a series of images and calculates the location of the
% moving droplet as it changes with time.

clear all; clc;

% Change each sample
directory='pattL_41cm_1';
surfacetype='patterned L2'; %match excel file name
sheet='41cm 1'; %line label in Results.xls, also sheet name in data file4
linenum='106'; %next empty line in Results.xls
first=1;
last=110;

y_pixels=399;
x_pixels=445;
leftmostpixel=113;% If you want to cut off a side, enter pixel locations
topmostpixel=1;

highframe='0001'; % Enter where the drop is high and low on the screen
lowframe='0040';  % 4 digits

% Change each set of samples
pixel_conversion=(1/40.38)/1000; %m/pixel
time_frame=1/6000; %seconds
fluid=3; %1-water, 2-alcohol, 3-gly/water mix

% surfaceedge=1;
```

```
% rightmostpixel=1;

% Get background image to subtract off
firstframe=[directory '/' directory '00' highframe '.jpg'];
lastframe=[directory '/' directory '00' lowframe '.jpg'];
x1=double(imread(firstframe));
x2=double(imread(lastframe));

resultlabel=['a' linenum];
resultline=['b' linenum];

i=0;
j=0;
backcut=300;
for i=1:1:y_pixels
   for j=1:1:x_pixels
      if i<=backcut
         background(i,j)=x2(i,j);
      end
      if i>backcut
         background(i,j)=x1(i,j);
      end
   end
end

for ii=first:1:last
ii
iis=int2str(ii);

%Read in image
if ii<10
   currentframe=[directory '/' directory '00' '000' iis '.jpg'];
end
if ii<100
   if ii>=10
      currentframe=[directory '/' directory '00' '00' iis '.jpg'];
   end
end
if ii<1000
   if ii>=100
      currentframe=[directory '/' directory '00' '0' iis '.jpg'];
   end
end
if ii<10000
   if ii>=1000
      currentframe=[directory '/' directory '00' iis '.jpg'];
```

```
   end
end
x1=double(imread(currentframe));
x1=(x1(1:y_pixels, 1:x_pixels));  %Downsizes windows

%Eliminate some noise
matrix_sub=abs(x1-background);
i=0; j=0;
for i=1:1:y_pixels
   x(i)=i;
   for j=1:1:x_pixels
      jj=y_pixels+1-j;
      if matrix_sub(i,j)<10 %increase value to eliminate more noise
         matrix_sub(i,j)=0;
      end
   end
end
i=0;
j=0;
for i=1:1:y_pixels    % Cut off noise
   for j=1:1:x_pixels
      if j<leftmostpixel  %cut off left side noise
         matrix_sub(i,j)=0;
      end
%        if j>rightmostpixel  %cut off right side noise
%           matrix_sub(i,j)=0;
%        end
%        if i>(y_pixels-surfaceedge)  %cut off surface noise
%           matrix_sub(i,j)=0;
%        end
      if i<topmostpixel  %cut off top noise
         matrix_sub(i,j)=0;
      end
   end
end

%displacement in the x direction
x_dis=0;
for i=1:1:y_pixels
   xpic_loc=0;
   iii=1;
     for j=1:1:x_pixels
        if matrix_sub(i,j)>0
           xpic_loc(iii)=j;
           iii=iii+1;
        end
```

```
      end
   x_dis_new=max(xpic_loc)-min(xpic_loc);
   if x_dis_new > x_dis
      x_dis=x_dis_new;
   end
end
x_dis_drop(ii)=x_dis;

%find the top edge of the droplet
jjj=1;
y_dis=0;
for i=1:1:y_pixels
   for j=1:1:x_pixels
      if matrix_sub(i,j)>=1
         y_dis(jjj)=i;
         jjj=jjj+1;
      end
   end
end
y_dis_drop(ii)=-min(y_dis);

y=y_pixels:-1:1;
x=1:1:x_pixels;

% figure(ii)
% contour(x,y,matrix_sub)

end

% % Display background image to see if it is adequate
% figure(1)
% image(background); colormap(gray(256)); axis('equal')

time=0:time_frame:(time_frame*(length(x_dis_drop)-2));

% Positions
i=0;
sx=0;
sy=0;
for i=1:1:(length(x_dis_drop)-1)
   sx(i)=x_dis_drop(i)*pixel_conversion;
   sy(i)=y_dis_drop(i)*pixel_conversion;
end

figure(2)
plot(time, sx, 'o', time, sy, 'x')
```

```
title('Positions')
xlabel('Time (s)')
ylabel('Position (m)')
legend('Horizontal Diameter','Height of Top','Location','SouthOutside')

clear x y;
data_process2(sx,sy,time_frame,surfacetype,sheet,resultline,first,fluid);

[XLS, label] = xlsfinfo([surfacetype '.xls']);
xlswrite('results.xls', label(size(label,2)), surfacetype, resultlabel);

sx=sx';
sy=sy';



% This function takes a data set from the droplet_track.m program and
% finds points of interest and curve-fits the data, to smooth it out.
% Created by John Pearson on 9/11/2008

function [vx,vy]=data_process(x,y,dt,surfacetype,sheet,resultline,first,fluid)

for i=first:1:first+2
   dydt(i)=(y(i+1)-y(i))/dt;
   dxdt(i)=(x(i+1)-y(i))/dt;
end
for i=size(x,2)-2:1:size(x,2)-1
   dydt(i)=(y(i+1)-y(i))/dt;
   dxdt(i)=(x(i+1)-y(i))/dt;
end

% Fit a curve to the x and y data at each point, find velocity
for i=first+3:1:size(x,2)-3
   dydt(i)=(y(i+1)-y(i))/dt;
   dxdt(i)=(x(i+1)-x(i))/dt;
   time=[dt*(i-2) dt*(i-1) dt*(i)];
   xval=[x(i-1) x(i) x(i+1)];
   yval=[y(i-1) y(i) y(i+1)];
   posx=polyfit(time,xval,2);
   xposition(i)=posx(1)*dt*(i-1)*dt*(i-1)+posx(2)*dt*(i-1)+posx(3);
   vx(i)=posx(1)*2*dt*(i-1)+posx(2);
   posy=polyfit(time,yval,2);
   yposition(i)=posy(1)*dt*(i-1)*dt*(i-1)+posy(2)*dt*(i-1)+posy(3);
   vy(i)=posy(1)*2*dt*(i-1)+posy(2);
end
```

```
% Write to file the position and velocity fits along with the raw data.
times=(0:dt:dt*size(x,2)-dt);
xlswrite([surfacetype '.xls'], times', sheet, 'a2');
xlswrite([surfacetype '.xls'], x', sheet, 'b2');
xlswrite([surfacetype '.xls'], xposition', sheet, 'c2');
xlswrite([surfacetype '.xls'], dxdt', sheet, 'd2');
xlswrite([surfacetype '.xls'], vx', sheet, 'e2');
xlswrite([surfacetype '.xls'], y', sheet, 'f2');
xlswrite([surfacetype '.xls'], yposition', sheet, 'g2');
xlswrite([surfacetype '.xls'], dydt', sheet, 'h2');
xlswrite([surfacetype '.xls'], vy', sheet, 'i2');

[XLS, label] = xlsfinfo('labels.xls');
xlswrite([surfacetype '.xls'], label, sheet, 'a1');

% Find impact velocity (probably won't work if there are discontinuities)
j=find(max(vx)==vx);
if j(1,1)<11
   u=-mean(vy(3:j(1,1)));
else
   u=-mean(vy(j(1,1)-8:j(1,1)));
end
[t_jet,t_maxD,j,xposvals,yvelvals]=timefind(first,x,y,dt,u);

if j(1,1)<11
   u=-mean(vy(3:j(1,1)));
else
   u=-mean(vy(j(1,1)-8:j(1,1)-1));
end

% Find droplet diameter prior to impact
iv=0;
for i=first:1:j(1,1)
   iv=iv+1;
   D(iv)=x(i);
end
d=mean(D);

% Find average velocity of spread
vavedata=find(max(x)==x);
vave=x(find(max(vx)==vx)-3:1:vavedata(1,1))-d;
vave=sum(vave)/(dt*(vavedata(1,1)-(j(1,1)-3)));

% Prepare dimensionless data to export to excel.
if fluid==1 %water
   rho=998;
```

```
   sigma=.0727;
   mu=.000959;
elseif fluid==2  %alcohol
   rho=789;
   sigma=.0228;
   mu=.00119;
else  %glycerine-water mixture
   rho=1126.3;
   sigma=.0692;
   mu=.006;
end
We=rho*u^2*d/sigma;
Re=rho*u*d/mu;
tmaxD=t_maxD*u/d;
tjet=t_jet*u/d;
maxD=max(x)/d;
v_jet=max(vy)/u;
v_spread=max(vx)/u;
v_ave=sum(vave)/u;

excel=[d u We Re tmaxD(1,1) tjet maxD(1,1) v_jet v_spread v_ave];

xlswrite('results.xls', excel, surfacetype, resultline);



% This function finds the impact, max diameter, and jet ejection times.
% Created by John Pearson on 1-27-09

function [tjet,tmaxD,impactframe,xposition,vy]=timefind(first,x,y,dt,u)
x=x;

i=0;
for i=first+3:1:size(x,1)-3
   time=[dt*(i-4) dt*(i-3) dt*(i-2) dt*(i-1) dt*(i) dt*(i+1) dt*(i+2)];
   xval=[x(i-3) x(i-2) x(i-1) x(i) x(i+1) x(i+2) x(i+3)];
   yval=[y(i-3) y(i-2) y(i-1) y(i) y(i+1) y(i+2) y(i+3)];
   posx=polyfit(time,xval,2);
   xposition(i)=posx(1)*dt*(i-1)*dt*(i-1)+posx(2)*dt*(i-1)+posx(3);
   vvx(i-2)=posx(1)*2*dt*(i-3)+posx(2);
   posy=polyfit(time,yval,2);
   vvy(i-2)=posy(1)*2*dt*(i-3)+posy(2);
   yet=0;
   while yet<1
   chkk=find(xposition==xposition(i));
   if size(chkk,2)>1
```

```
        xposition(i)=xposition(i)-0.000001;
    end
    if size(chkk,2)<2
        yet=12;
    end
    end
    yet=0;
    while yet<1
    chkk=find(vvy==vvy(i-2));
    if size(chkk,2)>1
        vvy(i-2)=vvy(i-2)-0.000001;
    end
    if size(chkk,2)<2
        yet=12;
    end
    end
end

%Find impact frame
for i=1:1:10
    ifr(i)=find(max(vvx)==vvx);
    vvx(ifr(i))=0;
end
ifrave=mean(ifr);
ifrstd=std(ifr);
idist=abs(ifr-ifrave);

for i=1:1:10
    if idist(i)>ifrstd
        ifr(i)=0;
    end
end

chk=0;
i=0;
while chk<1
    i=i+1;
    if ifr(i)>0
        impactframe=ifr(i)-round(max(0, -3.4286*u+6.2))-2;
        chk=2;
    end
end

%Find t_jet
for i=1:1:5
    jfr(i)=find(max(vvy)==vvy);
```

```
    vvy(jfr(i))=0;
end
jfrave=mean(jfr);
jfrstd=std(jfr);
jdist=abs(jfr-jfrave);

for i=1:1:5
    if jdist(i)>jfrstd*1.1
        jfr(i)=0;
    end
end

chk=0;
i=0;
while chk<1
    i=i+1;
    if jfr(i)>0
        tjet=(jfr(i)-impactframe)*dt;
        chk=2;
    end
end

%Find t_maxD
for i=1:1:10
    dfr(i)=find(max(xposition)==xposition);
    xposition(dfr(i))=0;
end
dfrave=mean(dfr);
dfrstd=std(dfr);
dist=abs(dfr-dfrave);

for i=1:1:10
    if dist(i)>dfrstd
        dfr(i)=0;
    end
end

chk=0;
i=0;
while chk<1
    i=i+1;
    if dfr(i)>0
        tmaxD=(dfr(i)-impactframe)*dt;
        chk=2;
    end
end
```

B.3 Codes for Analytical Models

```
% This program compares my data with Attane 2007 using a Runga Kutta method

clc; clear all;

% Parameters
surface='both L';
h=.00001; %timestep size
%get info from file
dataset=xlsread('comparisons.xls', surface);
theta=dataset(2:size(dataset,1),7)*pi/180;
We=dataset(2:size(dataset,1),8);
% Re=dataset(:,4);
pearson=dataset(:,7);
Oh=dataset(2:size(dataset,1),9);%(We.^(1/2))./Re;
s=1.41*Oh.^(-2/3);

%Set initial conditions
r0=dataset(:,16);
dr0dt=We.^(1/2)*(2/3+1/45*1/r0.^6).^(-1/2);

%Apply RK4 method on system of 2 eqns
for i=1:1:size(dataset,1)
   i
   clear r dr;
   r(1)=r0(i);
   dr(1)=dr0dt(i);
   signchange=0;
   j=0;
   while signchange<1
      j=j+1;

      x1=r(j);
      x2=dr(j);

      [T1, S1]=eqns(x1, x2, theta(i), Oh(i), s(i));

      x1=r(j)+.5*h*T1;
      x2=dr(j)+.5*h*S1;

      [T2, S2]=eqns(x1, x2, theta(i), Oh(i), s(i));

      x1=r(j)+.5*h*T2;
      x2=dr(j)+.5*h*S2;
```

```
        [T3, S3]=eqns(x1, x2, theta(i), Oh(i), s(i));

        x1=r(j)+h*T3;
        x2=dr(j)+h*S3;

        [T4, S4]=eqns(x1, x2, theta(i), Oh(i), s(i));

        r(j+1)=r(j)+h/6*(T1+2*T2+2*T3+T4);
        dr(j+1)=dr(j)+h/6*(S1+2*S2+2*S3+S4);

        if dr(j+1)<0
           signchange=10;
        end
    end
    beta_max(i)=max(r)*2;
    tmax_D(i)=j*h;
end

beta_max=beta_max';



function [k1, k2]=eqns(x1, x2, theta, Oh, s)

k1=x2;
k2=(1/90/x1^7*x2-2*x1*(1-cos(theta))+1/3/x1^2-4*Oh*(3*x1^...
          4+2/3/x1^2+s*x1)*x2)/(1/9+1/270/x1^6);
```